A Reference Section Through Fast-Spread Lower Oceanic Crust, Wadi Gideah, Samail Ophiolite (Sultanate of Oman): Insights From Crystallographic Preferred Orientations

Dominik Mock, Benoit Ildefonse, Tim Müller, Jürgen Koepke

JGR Solid Earth

RESEARCH ARTICLE
10.1029/2021JB021864

Special Section:
Ophiolites and Oceanic Lithosphere, with a focus on the Samail ophiolite in Oman

A Reference Section Through Fast-Spread Lower Oceanic Crust, Wadi Gideah, Samail Ophiolite (Sultanate of Oman): Insights From Crystallographic Preferred Orientations

Dominik Mock[1,2], Benoît Ildefonse[2], Tim Müller[1], and Jürgen Koepke[1]

[1]Institut für Mineralogie, Leibniz Universität Hannover, Hannover, Germany, [2]Géosciences Montpellier, Université de Montpellier, CNRS, Montpellier, France

Key Points:

- A Reference section through fast-spread lower oceanic crust was established with respect to microstructures
- Microstructural features of the lower oceanic crust of the Samail paleoridge vary with depth
- Data suggest a hybrid accretion model with different mechanisms for the upper and lower plutonic crust

Correspondence to:
D. Mock,
d.mock@mineralogie.uni-hannover.de

Citation:
Mock, D., Ildefonse, B., Müller, T., & Koepke, J. (2021). A reference section through fast-spread lower oceanic crust, Wadi Gideah, Samail ophiolite (Sultanate of Oman): Insights from crystallographic preferred orientations. *Journal of Geophysical Research: Solid Earth*, *126*, e2021JB021864. https://doi.org/10.1029/2021JB021864

Received 9 FEB 2021
Accepted 4 JUN 2021

Abstract We established a 5,000 m thick profile through the paleo lower oceanic crust of the Samail ophiolite (Sultanate of Oman, Wadi Gideah), in order to investigate accretion processes beneath fast-spreading mid-ocean ridges. The Samail ophiolite is regarded as best on-land analog for fast-spread oceanic crust, and Wadi Gideah allows sampling of the entire lower crust along the Wadi bed. Here, we provide microstructural constraints to lower crustal accretion beneath fast-spreading mid-ocean ridges, which reveal changing microstructures and fabrics with depth. Grain size coarsening occurs from the foliated to the layered gabbro section. A ~350 m thick zone of gabbroic rocks from the profile top, interpreted as frozen fillings of the axial melt lens and defined as varitextured gabbros, shows intergranular textures without crystallographic preferred orientations. Rocks from the varitextured/foliated gabbro transition (~500 m thick) and from the upper foliated gabbros (~600 m) are foliated and lineated. The lineation is absent or very weak in the underlying ~800 m thick lower foliated gabbros. In layered gabbros, the fabric gradually strengthens and becomes more lineated down section with local scattering at small spatial scales. This implies distinct accretion mechanisms in the deep and shallow plutonic crust. For the layered and lower foliated gabbros, our data suggest in-situ crystallizing individual magma reservoirs. Dominant lineation in the upper foliated gabbros and the varitextured/foliated gabbro transition suggests vertically transported crystal-laden melts or mushes being consistent with subsiding crystal mushes from the axial melt lens, and/or crystallizing upward migrating melt expelled from the crystal mush beneath.

Plain Language Summary "Ophiolites" are fragments of ancient oceanic crust and shallow mantle thrusted on land mainly during mountain building processes. They provide the potential for a deep understanding how the oceanic crust forms. The largest, best-preserved and best-investigated ophiolite on our planet is the Samail ophiolite in the Sultanate of Oman, where we performed our study. We sampled a continuous lower crustal section, consisting of gabbro, from the upper mantle up to the transition with the upper basaltic crust in Wadi Gideah, near the town of Ibra in Northern Oman, with the aim to understand its formation, which is up to now controversially discussed. We used the Electron Backscattered Diffraction technique for investigating the microstructures of the sampled rocks, enabling insights into the mechanism of magmatic emplacement of the lower crust. These microstructures reveal that the upper third of the lower crust is dominated by vertical transport of melt and magmatic mush, while the lower two thirds were formed by intrusions and in-situ crystallization.

1. Introduction

Based on marine geophysics, seafloor geology, and ophiolite studies, the classical picture of a uniformly layered oceanic crust (with basaltic lava flows, basaltic sheeted dikes, and gabbros, from top to bottom) emerged in the early 1970s (Anonymous, 1972). About 50 years later, our vision of the architecture of the ocean crust has considerably evolved, with a continuously growing understanding of its variability at the global scale. This variability results from various modes of accretion that are controlled by magma supply to the ridge, which in turn is related on the first order to spreading rate (e.g., Chen, 1992; Bown & White, 1994; Cannat et al., 2009; Coogan et al., 2007; Dick et al., 2003; Ildefonse et al., 2014; Karson et al., 2015).

A significant feature of the lower fast-spreading oceanic crust is a coherent modal layering. This is well-known from ophiolites since decades (Nicolas, 1989) and was studied in more details for the Samail ophiolite more recently, in order to shed light on the emplacement mechanism of deep crystal mushes and on the layer-forming processes (e.g., Jousselin et al., 2012; Mock, Neave, et al., 2020). The occurrence of modal layering in lower crustal gabbros was also confirmed in 2014 from recent fast-spread crust by an International Ocean Discovery Program Expedition into the lowermost crust at Hess Deep in the Eastern Pacific (Gillis, J. E. Snow et al., 2014). The steady-state axial magma reservoir, and related crustal accretion mechanism(s) that are necessary to account for the production of a continuous, layered crust at mid-ocean ridges, were first conceptualized as relatively large magma bodies, up to ∼10–20 km large across the ridge axis, and ∼4 km thick at the axis, lying below the sheeted dike complex (e.g., Cann, 1974; Nicolas et al., 1988; Pallister & Hopson, 1981). These models were largely constrained by observations made in ophiolites and were different in terms of magma chamber shape and symmetry (i.e., Δ-shaped in Cann, 1974 or V-shaped in Pallister & Hopson, 1981). Using thermal constraints, Sleep (1975) proposed that most of the chamber was filled with magmatic mush, and that melt-rich magma would be limited to the top, below the sheeted dykes. This prediction was confirmed a few years later, with the first seismic reflection images of the top of a thin axial magma chamber beneath the Valu Fa ridge in the Lau Basin (Morton & Sleep, 1985) and the East Pacific Rise (e.g., Detrick et al., 1987; Hale et al., 1982; Herron et al., 1980; Vera et al., 1990). Below this axial magma lens was pictured a seismically attenuated domain, which was inferred to correspond to a melt-poor magmatic mush (e.g., Caress et al., 1992; Dunn et al., 2000; Harding et al., 1989; Orcutt et al., 1976). About 30 years ago, two competing end-member models were then proposed for building the lower, gabbroic crust in this domain: the "gabbro glacier model" (Henstock et al., 1993; Phipps Morgan & Chen, 1993; Quick & Denlinger, 1993) postulates that the entire lower crust is formed by flow of mushy material downward and outward from the single, shallow axial magma lens, and the "sheeted sill model" focuses on in-situ formation of the lower crust by sill intrusions with a small region of cumulates from the axial melt lens (AML) beneath the sheeted dikes (Kelemen et al., 1997; Kelemen & Aharonov, 1998). A combination of these two end-member models was proposed by Boudier et al. (1996). While the gabbro glacier model does not require deep hydrothermal circulation close to the ridge axis, a deep cooling system is needed to sustain a sheeted sill model (e.g., Maclennan et al., 2005). Therefore, the estimation of cooling rates along the lower oceanic crust play a pivotal role in the evaluation of possible accretion mechanisms.

These accretion models can be used for predicting contrasted vertical trends of petrology, deformation, cooling rates, and alteration in the gabbroic crust (e.g., Ildefonse et al., 2010), which still remain to be fully tested in ophiolites and by deep drilling in intact fast-spread crust (e.g., Ildefonse et al., 2014; Teagle et al., 2012). Coogan et al. (2002, 2007) and Faak et al. (2015) investigated cooling rates as a function of depth in the Samail ophiolite and at the EPR, respectively, and found that the cooling rate decreases down section, as predicted by thermal modeling of Maclennan et al. (2005) for a conductively cooled gabbro glacier. They argue that the slow cooling rates, in particular within the lower crust of the Samail ophiolite (Coogan et al., 2002, 2007), do not facilitate in-situ crystallization because the latent crystallization heat is assumed to prevent a significant amount of crystallization in a slowly cooled environment.

Petrological studies in the Samail ophiolite suggest deep in-situ intrusions as the main accretion mechanism for the lower crust (e.g., Kelemen et al., 1997; Koepke et al., 2017; Müller, 2016). While Kelemen et al. (1997) studied gabbroic sills that intruded mantle rocks in the crust-mantle transition zone, and also used petrological data by Browning (1984), Müller (2016), and Koepke et al. (2017) sampled a profile over the entire lower crust along Wadi Gideah in the Wadi Tayin block. Along this profile, Mg#s in bulk rock, olivine and clinopyroxene, as well as the anorthite content in plagioclase show decreasing trends up section indicating melt fractionation along the lower crust, as expected to occur within crystallizing sills. The low, and down section decreasing cooling rates in the lower crust documented by Coogan et al. (2002, 2007) are inconsistent with the interpretation of sill crystallization at depth. In contrast, the variable faster cooling rates obtained for layered gabbros (LG) of the Samail ophiolite by VanTongeren et al. (2008) indicate that the thermodynamic requirement of latent heat removal from the lower crust enabling in-situ crystallization can be fulfilled.

Because rock fabrics provide helpful information on deformation processes, which in turn can be interpreted in terms of crustal accretion mechanisms, Nicolas et al. (2009) and Morales et al. (2011) investigated

microstructures in gabbros and anorthosites, respectively, from the root zone of the sheeted dyke complex and the underlying foliated gabbros (FG) in the Samail ophiolite. They found crystallographic preferred orientations (CPO) which indicate subsiding of a crystal mush from the AML, consistent with the gabbro glacier mechanism forming the upper part of the lower crust in the Samail ophiolite. This conclusion is consistent with the results of Brown et al. (2019), who analyzed microstructures in the upper 800 m of the recent lower oceanic crust from Pito Deep at the EPR. They propose that the analyzed gabbroic rocks crystallized within the AML and subsequently subsided from the AML downward to form at least the upper 800 m of the plutonic crust. Similarly, Perk et al. (2007) investigated the microstructures, petrology, and geochemistry of the uppermost 1,000 m below the sheeted dike complex at Pito Deep and concluded that gabbros might have crystallized at shallow depths, and subsequently subsided and formed the observed foliated and layered textures within the uppermost 1,000 m of the gabbros. However, they compare their data with those from Hess Deep and suggest that the formation of the latter may have occurred by subsiding crystal mush in the shallow part of the lower crust, and by in-situ crystallization deeper in the crust. VanTongeren et al. (2015) studied plagioclase CPO along the entire lower crust in Wadi Khafifah (Wadi Tayin block, Samail ophiolite) and found no down section trends, neither in fabric strength nor in lineation orientation that are predicted in the gabbro glacier model. Hence, their data support the sheeted sill model for the studied crustal section. Seismic experiments performed at the Juan de Fuca Ridge (Canales et al., 2009), the Galapagos Spreading Center (Boddupalli & Canales, 2019) and the EPR (Marjanovic et al., 2014, 2015) provide evidence for the occurrence of small melt sills within the lower crust supporting the possibility of in-situ crystallization beneath the spreading center. A weakness of most of the abovementioned studies is that they either cover only parts of the lower oceanic crust (e.g., Brown et al., 2019; Faak et al., 2015; Morales et al., 2011; Nicolas et al., 2009; Perk et al., 2007) or provide a relatively low spatial resolution along the crust (Coogan et al., 2002, 2007; VanTongeren et al., 2008, 2015) making well-founded, unequivocal interpretations in terms of lower crustal accretion difficult.

Our objective in this paper is to test fast-spread crust accretion models by quantifying the vertical variability of CPO and Crystal Size Distribution (CSD) of primary silicate phases (plagioclase, clinopyroxene, olivine) in gabbroic rocks, as a qualitative proxy for strain and cooling, in the lower oceanic crust Wadi Gideah in the Samail ophiolite (Garbe-Schoenberg et al., 2014; Koepke et al., 2017; Müller, 2016; Müller et al., 2014; Oeser et al., 2012). Our data provide a high spatial resolution along the entire gabbroic section exposed at Wadi Gideah. A further increase of the spatial resolution will also be reached in upcoming publications by integrating drill core data in the frame of the Oman Drilling Project (see below; Kelemen et al., 2020). For the drill sites within the layered gabbro and in the transition between layered and foliated gabbro, the Wadi Gideah was chosen because it displays a continuous crustal section from the crust/mantle boundary to the sheeted dike horizon in a region (the southern Wadi Tayin massif) that is arguably not disturbed by any secondary magmatic event such as large intrusions of wehrlites or gabbronorites (e.g., Goodenough et al., 2014), and which shows petrographic/petrologic features similar to gabbros from the East Pacific Rise (e.g., Koepke et al., 2011; Müller, Koepke, C. Garbe-Schoenberg, et al., 2017; Müller, Koepke, C. D. Garbe-Schoenberg, et al., 2017; Müller et al., 2014).

2. Geological Background: The Wadi Gideah Reference Section

The samples investigated here are a subset of a sample suite collected over four field campaigns along Wadi Gideah in the Wadi Tayin block of the Samail ophiolite (e.g., Nicolas et al., 2000; Pallister & Hopson, 1981, Figure 1), with the aim of constructing a complete analytical data set for a reference section in an analog to fast-spreading centers (Garbe-Schoenberg et al., 2014; Koepke et al., 2017; Müller, 2016; Müller et al., 2014; Oeser et al., 2012). Beside the microstructural data presented herein, the results of detailed petrographic and petrological, trace element and isotopic, as well as crystallization temperature studies will be published soon qualifying the Wadi Gideah section as a reference section of lower fast-spread crust in the Samail ophiolite. This reference section also provides the opportunity to integrate data from the drill cores GT1 and GT2 of the Oman Drilling Project (Kelemen et al., 2020), which are located in the same Wadi. The 400 m long gabbro sections from drill sites GT1 and GT2 are located in the LG and in the layered/foliated gabbro transition of the Wadi Gideah, respectively. Wadi Gideah drains southward from a divide located in the

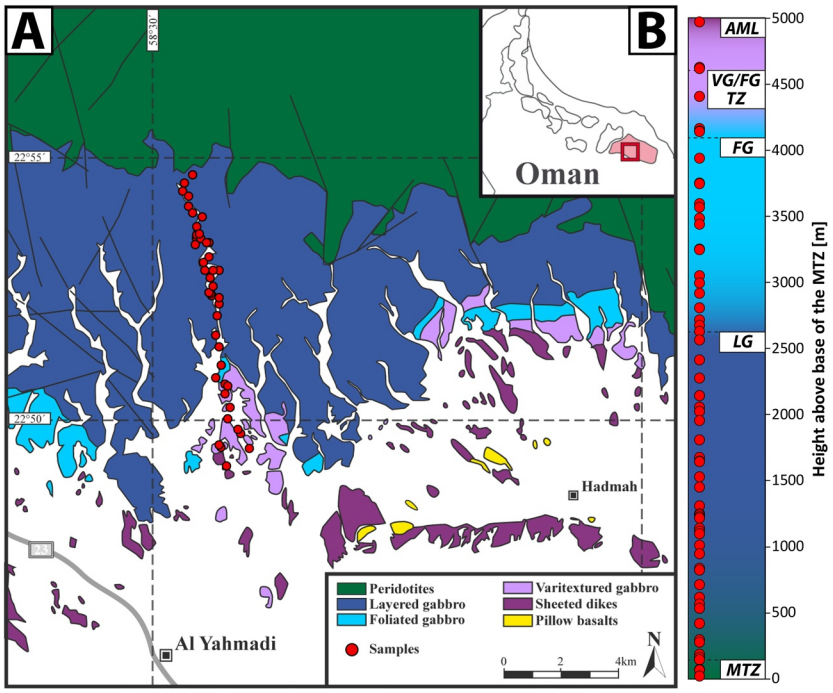

Figure 1. (a) Simplified geological map (modified after Peters et al., 2005) of the working area in the Wadi Gideah, Wadi Tayin massif, Samail ophiolite. Red circles mark locations of the analyzed samples along the Wadi, crossing the entire crustal sequence from the mantle transition zone to the sheeted dikes (see depth plot on the right for more details; AML, axial melt lens; VG/FG TZ, varitextured/foliated gabbro transition zone; FG, foliated gabbro; LG, layered gabbro; MTZ, mantle transition zone). (b) Overview of the entire ophiolite complex at the north-eastern coast of the Sultanate of Oman. The light red southernmost block is the Wadi Tayin massif, the red rectangle gives the cutout of (a).

harzburgites of the mantle horizon (Figure 1a). The crustal section dips gently ~28° to the south (Pallister & Hopson, 1981), a value which is representative of the whole Wadi Tayin block (Nicolas et al., 1996).

3. Materials and Methods

3.1. Sample Material

A subset of 68 samples (out of 293 samples for the whole reference section) was used for measuring CPO and CSD in this study (Table 1). The samples were initially obtained for geochemical analysis only and were not oriented in the field with respect to the structural context. They were cut perpendicular to the foliation and parallel to the lineation of the samples, when visible. The analyzed samples span the entire lower crustal section, with 44 samples from the lower, LG and the Moho transition zone (MTZ), 16 samples from the FG, five samples from a transition zone between varitextured and foliated gabbros (VG/FG TZ), and three samples which are considered to represent the frozen AML (e.g., Müller, Koepke, C. Garbe-Schoenberg, et al., 2017; Müller, Koepke, C. D. Garbe-Schoenberg, et al., 2017; Müller et al., 2017, Figure 1, Table 1). Wadi Gideah approximately parallels the inferred ridge axis which was mapped by Nicolas et al. (2000) about 10 km east of Wadi Gideah. The height above the base of the MTZ (in meters above MTZ; mam), was recalculated for each sample using the average 28° tilt of the section and the GPS coordinates of the sample locations. The vertical interval between each sample averages 81 m (and ranges from 1 to 389 m). Samples were not oriented in the field because they were initially taken for geochemical analyses. The foliation measured in the field indicate average dips of 26° and 74° to the South-West for the LG and FG, respectively, steepening from the lower to the upper FG (e.g., Nicolas et al., 1996, 2000; Pallister & Hopson, 1981; VanTongeren et al., 2015). This is consistent with the general structure of the gabbroic crust described in Oman, with sub-horizontal LG, subparallel to the crust-mantle boundary, and steep FG (e.g., Nicolas et al., 2000). Mineral foliations in the LG unit are subparallel to the dm-scale layering. The orientation of the modal layering was measured by Zihlmann et al. (2018) in a stratigraphic horizon <500 m above and

Journal of Geophysical Research: Solid Earth

10.1029/2021JB021864

Table 1
Fabric and Misorientation Data of the Primary Phases Plagioclase, Clinopyroxene, and Olivine of the Analyzed Samples Along Wadi Gideah Arranged by Height Above the Base of the MTZ

				Modal proportions (%)[d]						ODF J[e]			BA[f]			BC[f]		GOS[g]						GAM[h]					
Sample	Unit[a]	Lithology[b]	Height (mam)[c]	Pl	Cpx	Ol	Opx	Ox	sec	Pl	Cpx	Ol	Pl	Cpx	Ol	Pl	*std err*	Cpx	*std err*	Ol	*std err*	Pl	*std err*	Cpx	*std err*	Ol	*std err*
OM10_ Gid_A11	AML	Dol	4969	29.63	0.06	0.03	0	0.02	70.26	1.12								0.68	*0.01*	0.44	*0.06*	1.09	*0.26*	0.46	*0.00*	0.48	*0.06*	0.68	*0.12*
OM10_ Gid_ A12_2a	AML	an	4627	75.57	0.02	0.06	0.01	0.03	24.31	1.10								1.02	*0.01*	0.70	*0.08*	0.96	*0.19*	0.70	*0.00*	0.67	*0.10*	0.85	*0.13*
OM10_ Gid_ A12_2d	AML	dol	4627	54.72	0.08	0.1	0.01	0.03	45.07	1.09								0.74	*0.00*	0.39	*0.03*	0.69	*0.05*	0.56	*0.00*	0.41	*0.04*	0.50	*0.05*
OM10_ Gid_A13	VG/ FG TZ	ol-opx-hbl-b d-ox gb	4617	44.56	11	0.01	1.76	0.3	42.37	1.21	1.68		0.37					0.39	*0.01*	0.40	*0.01*	0.46	*0.05*	0.28	*0.00*	0.35	*0.00*	0.51	*0.14*
OM10_ Gid_A14a	VG/ FG TZ	ol-opx-hbl-b d-ox gb	4404	36.4	15.29	0.01	0.58	0.18	47.53	1.74	1.40		0.43	0.34		0.40	*0.00*	0.46	*0.01*	0.42	*0.06*	0.31	*0.00*	0.36	*0.00*	0.52	*0.07*
OM10_ Gid_A14b	VG/ FG TZ	hbl-ox-gb	4404	44.52	10.32	0.04	0	0.31	44.79	1.16	1.29		0.40	0.49		0.44	*0.00*	0.61	*0.01*	0.65	*0.05*	0.36	*0.00*	0.47	*0.00*	0.67	*0.05*
OM12_ Gid_214	VG/ FG TZ	ol-b d-ox gb	4161	34.89	14.88	1.36	0	0.24	48.61	1.39	1.28	3.86	0.24	0.35	0.68	0.39	*0.00*	0.38	*0.01*	0.31	*0.03*	0.34	*0.00*	0.30	*0.00*	0.26	*0.02*
OM10_ Gid_A15	VG/ FG TZ	hbl-ox-gb	4144	37.58	10.3	0.04	0	1.42	50.65	2.03	1.92		0.37	0.62		0.37	*0.00*	0.49	*0.01*	0.48	*0.09*	0.33	*0.00*	0.39	*0.00*	0.41	*0.05*
OM15_30	UFG	hbl-b d-ox gb	4138	14.69	6.84	0.11	0.01	0.75	77.61		1.95			0.53				0.40	*0.01*	0.63	*0.11*			0.32	*0.00*	0.60	*0.09*
OM10_ Gid_A16	UFG	hbl-opx-b d-ox ol-gb	3939	38.86	26.88	6.01	0.78	0.02	27.45	1.36	1.30	1.86	0.33	0.35	0.47	0.48	*0.00*	0.51	*0.01*	0.44	*0.02*	0.40	*0.00*	0.43	*0.00*	0.40	*0.00*
OM10_ Gid_A17	UFG	hbl-b ox-gb	3749	49.32	22.46	0.02	0	0.15	28.06	1.68	1.78		0.41	0.66		0.42	*0.01*	0.43	*0.01*	0.49	*0.06*	0.35	*0.00*	0.38	*0.01*	0.60	*0.13*
OM15_32	UFG	hbl-ox-gb	3747	51.95	19.15	0.03	0	1.07	27.79	1.34	1.68		0.52	0.52		0.53	*0.01*	0.45	*0.01*	1.07	*0.24*	0.35	*0.00*	0.32	*0.01*	0.75	*0.09*
OM10_ Gid_A17_2	UFG	hbl-b ox-gb	3592	33.78	23.87	0.04	0	0.08	42.22	1.39	1.97		0.45	0.27		0.68	*0.01*	0.70	*0.01*	0.60	*0.06*	0.50	*0.01*	0.60	*0.01*	0.58	*0.05*
OM10_ Gid_A17_1	UFG	hbl-b ox-gb	3565	53.98	18.1	0.13	0	1.53	26.25	1.31	1.69		0.52	0.77		0.56	*0.01*	0.60	*0.01*	0.66	*0.04*	0.41	*0.01*	0.48	*0.01*	0.66	*0.03*

Journal of Geophysical Research: Solid Earth

10.1029/2021JB021864

				Modal proportions (%)[d]						ODF J[e]			BA[f]	BC[f]		GOS[g]						GAM[h]					
Sample	Unit[a]	Lithology[b]	Height (mam)[c]	Pl	Cpx	Ol	Opx	Ox	sec	Pl	Cpx	Ol	Pl	Cpx	Ol	Pl	*std err*	Cpx	*std err*	Ol	*std err*	Pl	*std err*	Cpx	*std err*	Ol	*std err*
OM15_27	LFG	ol-opx-hbl-b d-ox gb	3486	46.63	31.5	0.76	2.31	0.44	18.36	2.09	2.50		0.36	0.43		0.29	*0.00*	0.38	*0.01*	0.66	*0.07*	0.20	*0.00*	0.29	*0.01*	0.47	*0.05*
OM10_Gid_A18	LFG	hbl-opx-box-ol-gb	3438	46.36	24.12	4.18	1.41	0.04	23.89	1.56	1.20	2.37	0.22	0.44	0.58	0.33	*0.00*	0.40	*0.01*	0.43	*0.01*	0.30	*0.00*	0.38	*0.00*	0.43	*0.01*
OM15_33	LFG	d-ox hbl-gb	3249	50.75	30.38	0.01	0.01	0.05	18.79	2.76	1.31		0.14	0.23		0.42	*0.00*	0.37	*0.01*	0.90	*0.18*	0.37	*0.00*	0.29	*0.00*	0.63	*0.11*
OM10_Gid_A18_1	LFG	Gb	3245	41.63	29.71	0	0	0	28.66																		
OM15_26	LFG	ol-gb	3048	34.93	36.18	9.02	0.12	0.04	19.71	4.22	2.18	5.08	0.15	0.22	0.17	0.29	*0.00*	0.29	*0.00*	0.48	*0.02*	0.24	*0.00*	0.23	*0.00*	0.30	*0.00*
OM12_Gid_217	LFG	ol-gb	2994	26.07	27.98	11.6	0.35	0.26	33.73	2.06	1.74	5.97	0.22	0.36	0.14	0.48	*0.01*	0.46	*0.01*	0.90	*0.03*	0.35	*0.00*	0.29	*0.00*	0.53	*0.02*
OM10_Gid_A18_2a	LFG	ol-gb	2915	43.88	26.98	3.07	0.43	0.01	25.64	2.44	1.26		0.15	0.41		0.36	*0.00*	0.57	*0.01*	0.52	*0.03*	0.25	*0.00*	0.34	*0.00*	0.35	*0.01*
OM12_Gid_218	LFG	ol-gb	2803	44.48	31.79	6.34	0.34	0.14	16.9	2.52	1.67	3.13	0.06	0.22	0.18	0.32	*0.00*	0.48	*0.02*	0.46	*0.02*	0.22	*0.00*	0.23	*0.00*	0.33	*0.01*
OM10_Gid_A19	LFG	ol-gb	2715	45.78	29.38	6.28	0.46	0.01	18.09	2.37	1.36	2.13	0.24	0.40	0.14	0.36	*0.00*	0.44	*0.00*	0.58	*0.03*	0.27	*0.00*	0.39	*0.00*	0.43	*0.01*
OM12_Gid_219	LFG	ol-gb	2671	49.87	35.11	6.47	0.78	0.07	7.71	2.26	1.36	2.15	0.38	0.50	0.44	0.27	*0.00*	0.27	*0.00*	0.38	*0.02*	0.25	*0.00*	0.24	*0.00*	0.31	*0.01*
OM12_Gid_57	LG	Gb	2625	48.29	32.19	0	0	0	19.5	1.60	2.23		0.32	0.23		0.26	*0.00*	0.29	*0.01*			0.24	*0.00*	0.26	*0.01*		
OM15_24	LG	ol-gb	2560	57.61	14.88	5.08	0.15	0.07	22.21	1.69		7.45	0.29		0.24	0.27	*0.00*			0.79	*0.09*	0.21	*0.00*			0.37	*0.01*
OM10_Gid_A20	LG	ol-gb	2409	46.59	22.02	5.11	0.11	0.01	26.17	2.06	2.67		0.29	0.38		0.31	*0.00*	0.39	*0.02*			0.27	*0.00*	0.33	*0.02*		
OM12_Gid_055	LG	ol-gb	2274	33.27	33.86	1.27	0.23	0.03	31.32	1.64	2.05		0.20	0.29		0.32	*0.01*	0.32	*0.01*			0.26	*0.00*	0.29	*0.00*		
OM10_Gid_A21	LG	ol-gb	2139	41.9	23.07	0.55	0.01	0.01	34.46	2.14	3.31		0.30	0.31		0.51	*0.01*	0.50	*0.01*			0.43	*0.00*	0.46	*0.01*		
OM11_Gid_A21a	LG	ol-b d-ox gb	2139	42.35	24.99	0.27	0.05	0.32	32.01	2.96	3.21		0.57	0.45		0.51	*0.01*	0.62	*0.02*			0.37	*0.00*	0.42	*0.01*		
OM12_Gid_054	LG	ol-b gb	2055	43.49	34.15	0.98	0.19	0	21.19	2.11	2.14		0.32	0.34		0.28	*0.01*	0.32	*0.01*			0.23	*0.00*	0.26	*0.00*		
OM12_Gid_052	LG	Gb	2019	35.08	20.01	0.01	0	0	44.89	5.05	4.26		0.49	0.48		0.61	*0.01*	0.58	*0.02*			0.50	*0.01*	0.45	*0.01*		
OM12_Gid_053	LG	ol-gb	2019	44.36	32.39	3.35	0.04	0.01	19.84	1.89	4.20		0.28	0.23		0.43	*0.01*	0.61	*0.05*			0.32	*0.00*	0.43	*0.03*		

Journal of Geophysical Research: Solid Earth

10.1029/2021JB021864

Sample	Unit[a]	Lithology[b]	Height (mam)[c]	Modal proportions (%)[d]						ODF J[e]			BA[f]			BC[f]				GOS[g]				GAM[h]					
				Pl	Cpx	Ol	Opx	Ox	sec	Pl	Cpx	Ol	Pl	Cpx	Ol	Pl	*std err*	Cpx	*std err*	Ol	*std err*	Pl	*std err*	Cpx	*std err*	Ol	*std err*
OM11_Gid_A22	LG	ol-gb	1951	50.32	29.85	2.68	0.17	0	16.98	2.39	2.47		0.34	0.46		0.25	*0.00*	0.39	*0.01*			0.23	*0.00*	0.28	*0.00*		
OM12_Gid_048	LG	ol-gb	1807	57.21	25.26	3.21	0.09	0	14.24	2.45	2.08	4.42	0.28	0.35	0.31	0.31	*0.00*	0.44	*0.01*	0.60	*0.04*	0.25	*0.00*	0.38	*0.00*	0.49	*0.01*
OM10_Gid_A23	LG	ol-b gb	1674	56.2	28.88	0.01	0	0	14.92	3.13	2.34		0.25	0.41		0.32	*0.00*	0.46	*0.01*			0.28	*0.00*	0.35	*0.01*		
OM12_Gid_045	LG	Gb	1645	29.55	33.87	0	0	0.11	36.47	2.15	3.58		0.48	0.41		0.45	*0.01*	0.44	*0.01*			0.34	*0.00*	0.32	*0.01*		
OM12_Gid_044	LG	ol-gb	1642	50.3	23.87	5.69	0.09	0	20.05	1.95	2.51	4.91	0.56	0.56	0.41	0.40	*0.01*	0.46	*0.02*	0.77	*0.04*	0.31	*0.00*	0.34	*0.01*	0.58	*0.01*
OM12_Gid_040	LG	Gb	1523	40.32	34.39	0	0.01	0	25.29	2.45	2.32		0.38	0.53		0.40	*0.01*	0.74	*0.03*			0.32	*0.00*	0.56	*0.02*		
OM10_Gid_A24	LG	ol-gb	1446	43.14	29.37	5.99	0.12	0	21.36	2.84	2.34	4.34	0.48	0.56	0.19	0.39	*0.01*	0.56	*0.02*	1.31	*0.07*	0.30	*0.00*	0.42	*0.01*	0.62	*0.02*
OM12_Gid_039	LG	ol-gb	1304	51.59	25.1	9.44	0.17	0	13.7	3.48	2.42	2.82	0.35	0.47	0.19	0.41	*0.01*	0.45	*0.01*	0.86	*0.03*	0.32	*0.00*	0.36	*0.00*	0.56	*0.01*
OM12_Gid_026	LG	Gb	1246	49.47	27.47	0	0.05	0.04	22.97	2.43	3.97		0.78	0.81		0.49	*0.01*	0.55	*0.02*			0.38	*0.00*	0.40	*0.01*		
OM12_Gid_027	LG	ol-opx-b gb	1237	43.5	19.17	1.47	4.59	0.01	31.25	2.23	4.84		0.61	0.40		0.33	*0.00*	0.39	*0.01*			0.29	*0.00*	0.38	*0.01*		
OM10_Gid_A25	LG	ol-gb	1225	41.38	27.9	6.75	0.05	0	23.91	2.55	2.64	5.44	0.57	0.58	0.49	0.40	*0.01*	0.59	*0.02*	1.25	*0.09*	0.35	*0.00*	0.50	*0.01*	0.70	*0.02*
OM12_Gid_025	LG	ol-b gb	1212	58.54	18.75	1.89	0.09	0	20.73	3.93	2.87		0.47	0.68		0.36	*0.01*	0.58	*0.04*			0.28	*0.00*	0.34	*0.01*		
OM12_Gid_038	LG	ol-gb	1136	51.71	18.11	12.63	0.35	0	17.2	2.31	2.60	2.08	0.48	0.56	0.46	0.39	*0.01*	0.46	*0.02*	0.71	*0.03*	0.34	*0.00*	0.34	*0.01*	0.53	*0.01*
OM15_1	LG	opx-b ol-gb	1134	47.09	21.73	5.01	0.19	0	25.97	2.86	2.66	5.49	0.33	0.49	0.27	0.33	*0.01*	0.43	*0.02*	0.71	*0.06*	0.27	*0.00*	0.27	*0.01*	0.40	*0.01*
OM15_2	LG	opx-b ol-gb	1114	51.64	22.59	7.56	1.09	0.01	17.11	2.32	2.12	4.52	0.40	0.38	0.23	0.42	*0.01*	0.42	*0.02*	1.19	*0.08*	0.32	*0.00*	0.28	*0.01*	0.57	*0.02*
OM10_Gid_A26	LG	ol-gb	1094	48.63	34.61	3.47	0.06	0	13.23	2.30	3.68		0.57	0.71		0.37	*0.01*	0.55	*0.02*			0.31	*0.00*	0.50	*0.01*		
OM12_Gid_035	LG	Gb	1006	0.76	22.01	0	0	0.58	76.65																		
OM11_Gid_A26	LG	ol-gb	945	49.27	27.09	2.82	0.03	0	20.8																		
OM11_Gid_A27	LG	ol-gb	831	38.7	27.78	10.21	0.17	0	23.13	2.72	2.50	2.89	0.44	0.52	0.34	0.43	*0.01*	0.59	*0.02*	1.12	*0.05*	0.39	*0.00*	0.42	*0.01*	0.67	*0.01*

Journal of Geophysical Research: Solid Earth
10.1029/2021JB021864

Sample	Unit[a]	Lithology[b]	Height (mam)[c]	Modal proportions (%)[d]						ODF J[e]			BA[f]			BC[f]			GOS[g]					GAM[h]					
				Pl	Cpx	Ol	Opx	Ox	sec	Pl	Cpx	Ol	Pl	Cpx	Ol	Pl	*std err*	Cpx	*std err*	Ol	*std err*	Pl	*std err*	Cpx	*std err*	Ol	*std err*
OM10_Gid_A27	LG	Gb	819	42.33	33.67	0.01	0	0	23.98	3.71	2.29		0.37	0.44		0.66	*0.01*	0.65	*0.02*			0.44	*0.00*	0.40	*0.01*		
OM10_Gid_A28	LG	Gb	711	39.6	34.18	0	0	0	26.22	2.85	3.31		0.67	0.79		0.81	*0.01*	0.80	*0.03*			0.59	*0.01*	0.52	*0.01*		
OM12_Gid_201	LG	ol-gb	613	35.58	31.01	9.02	0.3	0	24.09	2.59	2.50	3.07	0.47	0.40	0.15	0.54	*0.01*	0.64	*0.02*	0.96	*0.03*	0.42	*0.00*	0.38	*0.01*	0.61	*0.01*
OM10_Gid_A29	LG	Gb	560	36.29	32.91	0	0	2.03	28.77	2.54	1.59		0.56	0.62		0.57	*0.01*	0.66	*0.01*			0.45	*0.00*	0.48	*0.00*		
OM11_Gid_A29	LG	ol-gb	532	47.73	18.2	3.96	0.16	0	29.96	3.12	2.27	2.38	0.39	0.39	0.70	0.52	*0.01*	0.59	*0.02*	0.89	*0.04*	0.40	*0.00*	0.42	*0.01*	0.61	*0.01*
OM11_Gid_A29_2	LG	ol-gb	416	38.1	25.64	5.02	0.19	0	31.05	1.96	3.60	4.01	0.60	0.65	0.48	0.41	*0.01*	0.55	*0.02*	1.13	*0.07*	0.35	*0.00*	0.42	*0.01*	0.65	*0.02*
OM15_10	LG	ol-gb	291	38.1	37.76	1.64	0.01	0.01	22.48	2.45	1.84	7.41	0.49	0.42	0.34	0.45	*0.01*	0.53	*0.01*	0.75	*0.06*	0.31	*0.00*	0.29	*0.00*	0.42	*0.02*
OM10_Gid_A30	LG	ol-b gb	272	45.36	20.96	1.25	0.01	0.51	31.91	2.39	2.54	5.16	0.56	0.46	0.29	0.80	*0.01*	0.75	*0.02*	0.71	*0.05*	0.53	*0.01*	0.51	*0.01*	0.52	*0.02*
OM15_21	LG	Tr	180	53.29	0.11	8.84	0	0.12	37.63	2.52		3.89	0.49		0.41	0.61	*0.01*			0.99	*0.03*	0.40	*0.00*			0.59	*0.01*
OM15_15C_II	MTZ	Gb	157	43.73	27.29	0	0	1.99	27	2.91			0.46			0.46	*0.01*					0.33	*0.00*				
OM15_15D_II	MTZ	Gb	157	48.23	33.97	0	0.02	1.06	16.7	2.18	3.59		0.49	0.49		0.61	*0.01*	0.87	*0.04*			0.43	*0.01*	0.56	*0.01*		
OM10_Gid_A31	MTZ	ol-gb	138	50.23	24.67	3.98	0.3	0	20.82	2.95	1.90	3.52	0.61	0.67	0.32	0.50	*0.01*	0.63	*0.01*	0.67	*0.02*	0.30	*0.00*	0.42	*0.00*	0.52	*0.01*
OM15_18	MTZ	ol-b gb	65	44.03	35.69	1.96	0.18	0	18.13	2.44	1.46	3.51	0.35	0.41	0.35	0.39	*0.01*	0.44	*0.01*	0.51	*0.03*	0.23	*0.00*	0.24	*0.00*	0.30	*0.01*
OM10_Gid_A32	MTZ	ol-gb	64	45	23.14	5.57	1.41	0	24.87	1.94	1.42	2.54	0.68	0.64	0.26	0.45	*0.01*	0.48	*0.01*	0.56	*0.02*	0.28	*0.00*	0.36	*0.00*	0.35	*0.00*
OM15_13_II	MTZ	Tr	61	40.99	0.79	3.78	0.03	0.07	54.34	2.27			0.18			0.42	*0.01*					0.35	*0.00*				
OM15_19AII	MTZ	ol-gb	16	59.2	26.3	7.06	0.56	0	6.88	2.68	1.80	3.03	0.53	0.60	0.27	0.38	*0.01*	0.43	*0.01*	0.48	*0.02*	0.28	*0.00*	0.31	*0.00*	0.35	*0.01*

[a]Geological unit where the sample was taken. AML, axial melt lens; VG/FG TZ, varitextured/foliated gabbro transition zone; UFG, upper foliated gabbro; LFG, lower foliated gabbro; LG, layered gabbro; MTZ, mantle transition zone. [b]Lithology estimated by primary modal proportions after Gillis, J. Snow, et al. (2014) with ol, olivine; opx, orthopyroxene; ox, oxide; hbl, hornblende; gb, gabbro, tr, troctolite; an, anorthosite; dol, dolerite; b–, bearing (1%–5%); d–, disseminated (1%–2%) c crustal height of the sample in meters above the Moho. [c]Crustal height of the sample in meters above the Moho. [d]Phase proportions in percentage of all acquired pixels; pl, plagioclase; cpx, clinopyroxene; ol, olivine; opx, orthopyroxene; ox, oxides (ilmenite and magnetite); sec, summarized secondary alteration phases (hornblende, chlorite, actinolite); note that oxides may also be secondary products of serpentinization. [e]J index of the orientation distribution function quantifying the fabric strength of the phase per sample with 1 = random fabric and infinity = single crystal; J index of Pl and Cpx have been calculated using grain data, J index of olivine was calculated using grid data. [f]BA or BC index quantifying the pole figure symmetry of plagioclase and clinopyroxene, respectively. Varies between 0 and 1 with 0 = purely foliated and 1 = purely lineated symmetry; BA of Pl and Cpx have been calculated using grain data, BA of olivine was calculated using grid data. [g]Grain orientation spread calculated as the angle between the crystallographic orientation of an individual pixel and the crystallographic orientation of the corresponding grain averaged per phase and sample. [h]Grain average misorientation calculated as the average misorientation between individual pixel and its four nearest neighbored pixels averaged per phase and sample italic values are standard errors (std err) of the corresponding GOS or GAM, respectively empty cells belong to data sets which have not been used for plots due to bad data quality or a general lack of grains.

below a large fault zone at approximately 1,200 mam in Wadi Gideah and is 154/38° dipping to the South-East. This is consistent with previous field studies in the Wadi Tayin massif (e.g., Pallister & Hopson, 1981). Regardless of the dm-scale modal layering, which can hardly be observed in thin sections, LG and FG can be distinguished at the thin section scale by their grain size, which is ∼200 μm on average for plagioclase in the foliated and ∼310 μm on average in the LG. The LG transition to FG upward, at about 2,600 mam, through a diffuse, <100 m thick zone where LG and FG are mixed, and where the foliation rapidly steepens, as commonly described in many sections of the ophiolite (e.g., MacLeod & Yaouancq, 2000). Up-section, FG give way to varitextured gabbros (VG) from ∼4,150 mam. These isotropic rocks are called "varitextured" due to their strong heterogeneity in texture. They are highly variable in grain size, texture and chemical/modal composition (e.g., France et al., 2009; MacLeod & Yaouancq, 2000).

3.2. Crystallographic Preferred Orientations

Plagioclase, clinopyroxene, and olivine CPO were measured using the Electron Back-Scattered Diffraction (EBSD) technique (e.g., Prior et al., 2009), using a JEOL JSM-5600 Scanning Electron Microscope (SEM) at Géosciences Montpellier. The system is equipped with an Oxford/Nordlys EBSD detector; the diffraction patterns were collected using the Channel 5® software suite, and later the AZtec software from Oxford Instruments. The SEM was used at an accelerating voltage of 15 kV. Crystallographic orientation maps were obtained for each sample, covering about 80% of a thin section (2.5 × 4 cm) with a sampling step size ranging from 14 to 35 μm. The indexing rate (fraction of patterns that are automatically indexed during mapping) ranges from ∼25% to 94% in the raw maps (75% on average). The raw data contains all indexed pixels with a mean angular deviation (i.e., the angle between the acquired diffraction pattern and the indexing solution proposed by the software) ≤1°. A first stage of post-acquisition data processing was done using the Tango software of the Channel 5® suite to increase the quality of the maps. It consists of removing isolated pixels (either non-indexed or indexed as a given phase and surrounded by pixels indexed for another phase) and filling non-indexed pixels that have a minimum of 5 neighbor pixels with the same orientation. The EBSD data sets were then processed using MTEX (version 5.2.3), a free MATLAB toolbox for analyzing and modeling crystallographic orientations (http://mtex-toolbox.github.io; Bachmann et al., 2010; Hielscher & Schaeben, 2008). We used MTEX to identify grains and produce maps from the EBSD data, calculate pole figures of plagioclase, clinopyroxene, and olivine, analyze the crystallographic misorientations within grains, and calculate CPO strength and symmetry indices. A minimum of 100 grains is required to provide accurate fabric strength analyses (Ismail & Mainprice, 1998). We therefore plotted only data and contoured pole figures from measurements were at least 100 grains of a phase have been analyzed.

Grains were identified from the EBSD data by choosing a 10° threshold, over which the misorientation between two adjacent pixels indexed for the same phase is assumed to be a grain boundary. Grains that have a surface smaller than five pixels could be erroneous measurements and were removed from the data set. Twins in plagioclase have been distinguished from grain boundaries by filtering out the 180° (±5°) misorientations between adjacent grains around the twin rotation axes (crystallographic axes and poles [100], [100], [010], [010], [001], and [001]). Twins in clinopyroxene have been distinguished from grain boundaries by filtering out the 180° (±5°) misorientations between adjacent grains around the crystallographic axes (100) and (001). Pole figures were calculated using both the pixel data set from EBSD map data, and the average crystallographic orientation for each grain or each twinned domain in case of twinned grains. The second option can be preferred to avoid the overrepresentation of larger grains when the grain size distribution is heterogeneous at the thin section scale. We used this second option for clinopyroxene and plagioclase, and the pixel data (first option) for olivine. The intense mesh-serpentinization of olivine leads to misguided separation of primary grains into several "subgrains." Therefore, the average orientation option is misleading for olivine. The CPO strength for each phase is determined using both the J index (J) of the Orientation Distribution Function that is exclusively based on crystallographic orientations (e.g., Bunge & Bunge, 1982; Mainprice & Silver, 1993), and the M-index (Skemer et al., 2005), based on the misorientation angle distribution. J varies between 1 (for a uniform distribution) and infinite (for a single crystal); M varies from 0 to 1 (see Mainprice et al., 2015, for the details of J and M calculations and for a comparison between these two indexes). The Orientation Distribution Function was calculated using the "de la Vallee Poussin" kernel with a halfwidth of 10° (Schaeben, 1999; Mainprice et al., 2015).

The symmetry of the CPOs is determined using the BA-index (BA) for plagioclase and BC-indices (BC) for clinopyroxene and olivine, which are calculated from the Point (P), Girdle (G), and Random (R) indices that are themselves calculated from the eigenvalues ($\lambda_1 \geq \lambda_2 \geq \lambda_3$, with $\lambda_1 + \lambda_2 + \lambda_3 = 1$) of the orientation tensor for each pole figure (Mainprice et al., 2015; Satsukawa et al., 2013; Vollmer, 1990):

$$P = \lambda_1 - \lambda_3, G = 2\left(\lambda_2 - \lambda_3\right), R = 3\lambda_3, \tag{1a}$$

$$\mathrm{BA} = \frac{1}{2}\left[2 - \left\{\frac{P_{(010)}}{\left(G_{(010)} + P_{(010)}\right)}\right\} - \left\{\frac{P_{[100]}}{\left(G_{[100]} + P_{[100]}\right)}\right\}\right], \tag{1b}$$

$$\mathrm{BC} = \frac{1}{2}\left[2 - \left\{\frac{P_{(010)}}{\left(G_{(010)} + P_{(010)}\right)}\right\} - \left\{\frac{P_{[001]}}{\left(G_{[001]} + P_{[001]}\right)}\right\}\right]. \tag{1c}$$

In a plagioclase CPO that results from magmatic flow, the foliation is classically marked by a preferred orientation of planes (010), and the lineation by a preferred orientation of axes [100] (e.g., Mock, Neave, et al., 2020; Satsukawa et al., 2013). BA is 0 for a perfect axial-B CPO, an oblate (planar) fabric defined by a strong point alignment of (010) with a girdle distribution of [100], and it is 1 for a perfect axial-A CPO, a prolate (linear) fabric with a strong point maximum concentration of [100], and parallel girdle distributions of (010) and (001). BA is 0.5 for the intermediate p-type CPO with point maxima in [100], (010), and (001) (Satsukawa et al., 2013). With pyroxene and olivine, the situation is similar, except for the magmatic lineation that is then marked by the preferred orientation of [001] axes. Hence we use BC, to characterize the variations between a perfect oblate (BC = 0) and a perfect prolate (BC = 1) CPO. BA and BC are only presented for those samples that show a significant CPO. Therefore, a few samples with pole figures indicating no fabric are not included into BA or BC plots.

In EBSD maps, the misorientation within grains is quantified using four parameters, the misorientation to the mean (M2M), the grain orientation spread (GOS), the kernel average misorientation (KAM), and the grain average misorientation (GAM). M2M is, for each pixel within a grain, the angle between the crystallographic orientation of that pixel and the average crystallographic orientation of the grain. It visualizes the misorientation between domains separated by subgrain boundaries or the progressive misorientation related to undulose extinction in optical microscopy. The GOS is, for each grain, the average M2M. The KAM is, for each pixel, the average misorientation (lower than 10°) of the nearest n neighbors ($n = 4$ here, see Wright et al., 2011 for a review of misorientation parameters). The GAM is, for each grain, the average KAM.

3.3. Crystal Size Distributions

For the determination of CSD, we used the software CSDCorrections 1.60 provided by Higgins (2000). The inserted parameters length, width, area and angle of every plagioclase crystal were obtained by EBSD measurements. We used the ellipse minor axis length for the calculation. An average value of the plagioclase roundness was calculated from the EBSD data used for the CSD determination with the software. On the basis of the two-dimensional (2D) data obtained for every indexed grain, we calculated the three-dimensional (3D) aspect ratio of plagioclase following the procedure proposed by Higgins (1994) normed to 1 for the short axis length. Using the equation

$$\frac{L_{\mathrm{Intermediate}}}{L_{\mathrm{Short}}} = \frac{l}{w} \tag{2}$$

where L is the 3D length of the indexed parameter, l is the 2D length, and w the 2D width of the grain, the ratio of the 3D intermediate to short axis was calculated for every plagioclase grain with a width of at least

30 μm (=thin section thickness; cf., Higgins, 2000). For calculating the 3D long axis length, we used the skewness defined by

$$\text{skewness} = \frac{\left(\text{mean}\left(w/l\right)_{2D} - \text{mode}\left(w/l\right)_{2D}\right)}{\text{SD}\left(w/l\right)_{2D}}. \quad (3)$$

(Higgins, 1994) where $(w/l)_{2D}$ is the ratio of the 2D parameters width to length and *SD* is the standard deviation. The ratio of the 3D intermediate to long axes lengths could be determined using Figure 5 in Higgins (1994). Hence, the 3D long axis length was calculated by division of the 3D intermediate length (obtained from Equation 2) by the 3D intermediate to long axis ratio (obtained from Equation 3). With these data, a first calculation of the CSD was performed for a massive fabric. The resulting alignment factor was then used as qualifier of fabric (i.e., lineation intensity) for a second CSD calculation taking the previously calculated lineation intensity into account.

4. Results

The parameters calculated from the EBSD data are presented for plagioclase, clinopyroxene, and olivine in the Table S1 (Mock et al., 2020b). Examples of maps from varitextured, foliated and LG are presented in Figure 2.

4.1. General Observations

The lithological units are defined following previous field studies (e.g., Pallister and Hopson, 1981; Nicolas et al., 1996), and are consistent with field observations along the Wadi Gideah section (Garbe-Schoenberg et al., 2014; Koepke et al., 2017; Müller, 2016; Müller et al., 2014; Oeser et al., 2012). The samples located between 4,969 and 4,627 mam, which we interpret as frozen fillings of the dynamic AML are fine-grained, isotropic gabbros which we named dolerite in this study, and one anorthosite in sample OM10_Gid_A12_2a (Table 1). Below the AML, the VG transition to the FG unit over the VG/FG TZ from 4,617 to 4,144 mam. Olivine gabbros and olivine-bearing gabbros with occasional poikilitic hornblende or clinopyroxene containing plagioclase and variable grain sizes characterize this unit. Orthopyroxene and granular oxides are present in some of the samples. Both hornblende and oxide are also present in the underlying FG unit from 4,138 to 2,671 mam, which mainly consist of plagioclase and clinopyroxene. Some relicts of highly altered olivine and small amounts of orthopyroxene in some samples complete the mineral compositions in the FG unit. These rocks show a strong foliation and their grain sizes are constantly smaller than below within the LG unit. The occurrence of oxides, hornblende, and orthopyroxene systematically decreases down section in the FG unit. These phases are nearly absent in the LG unit below, which is dominated by mainly olivine gabbros with minor gabbro from 2,625 to 180 mam. The average grain size of the LG unit is clearly higher than in the FG unit, and their fabric is not only foliated but also shows an increasing lineation intensity down section. Samples from the MTZ come from 157 to 16 mam and show gabbro, olivine gabbro and troctolite. They have variable grain sizes, locally with cm-sized plagioclase and clinopyroxene. Their fabric symmetry reveals both foliation and lineation, which are best-defined by plagioclase preferred orientations.

As shown in Figures 2 and 3a, secondary phases (e.g., actinolite, chlorite, and hornblende) represent a significant fraction of the modal composition, indicating a degree of alteration between 10% and 80% that decreases down section. In particular, the olivine content (up to 16.7%) has to be taken with caution since olivine is highly sensitive to serpentinization leading to the underestimation of the primary olivine abundance by the EBSD. Regardless of the sensitivity of olivine to serpentinization and the increasing degree of alteration up section, the primary olivine content decreases up section, as observed petrographically. Along the entire crust, plagioclase (15%–76%) and clinopyroxene (0%–38%) form the most abundant primary phases, both showing significant variability along the sampled section. Orthopyroxene was found in several samples with low abundances (up to 6% in a single sample from the LG unit); it is more abundant in the FG and VG units. The primary oxide content (magnetite and ilmenite) is generally low, reaching a maximum of 1.5% in sample OM10-Gid-A17-1 within the FG unit. The abundance

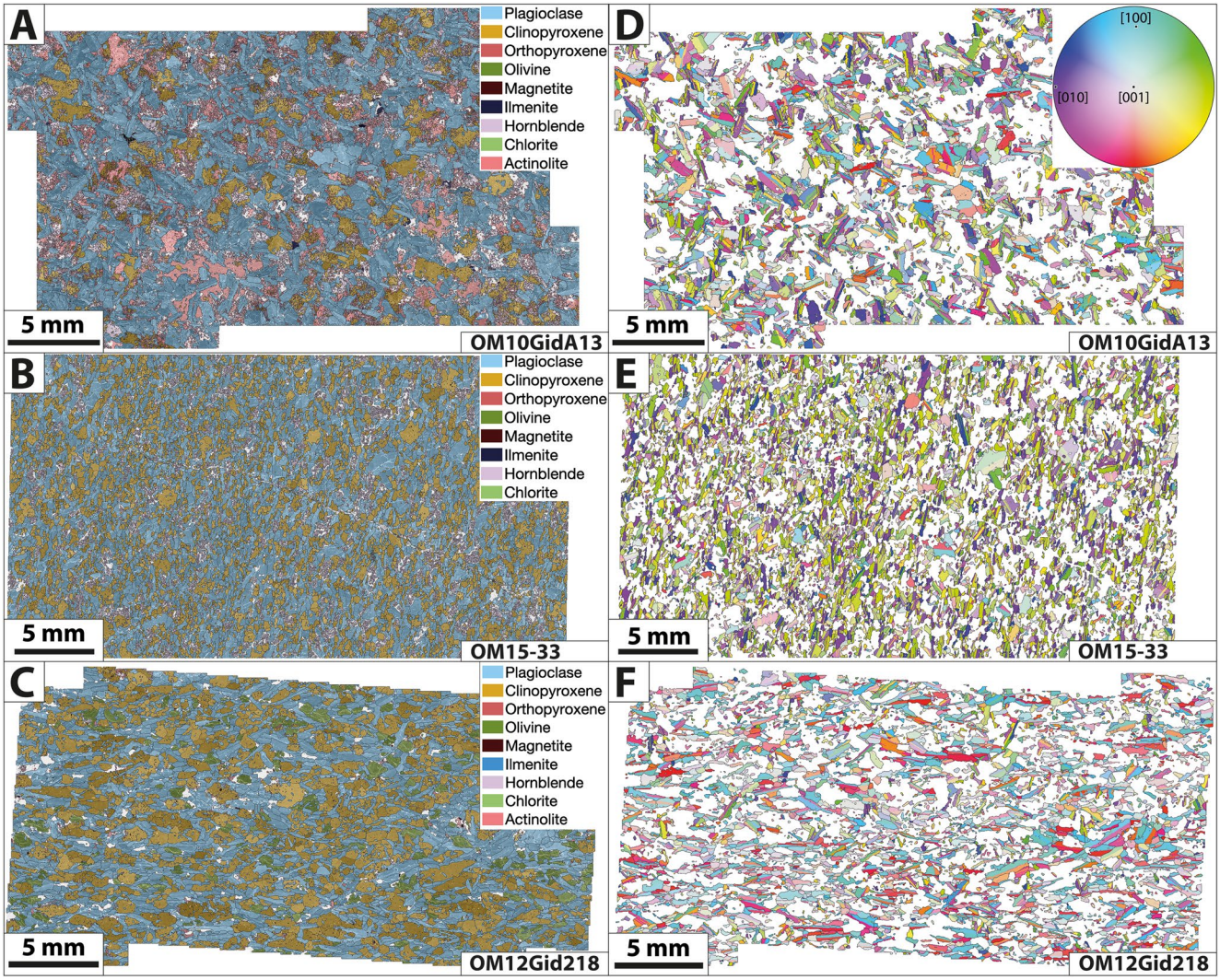

Figure 2. (a)(c) Phase maps acquired by EBSD representing a varitextured gabbro (a), a foliated gabbro (b), and a layered gabbro (c). (d) and (f) orientation maps of plagioclase from the same samples. The inverse pole figure color coding uses the *x* axis of the maps (horizontal) as a reference direction. Sample names and scale bars are given at the base of each image.

of secondary phases, hence the degree of alteration, increases above 3,000 mam at the expense of the primary major components plagioclase and clinopyroxene, which both show decreasing contents above 3,000 mam. Grain size (Figure 3b) is given by the diameter of the equivalent circle (i.e., with the same area as the corresponding grain). Plagioclase and clinopyroxene grain sizes are significantly coarser in the LG unit (beneath 2,600 mam) compared to the FG unit and the VG/FG TZ (Figure 3b). The plagioclase average grain size in the VG/FG TZ and FG unit is about 200 μm; it increases to 310 μm in the LG unit beneath 2,600 mam. Clinopyroxene forms coarser grains with 258 μm on average above 2,600 mam, and 410 μm on average below. The deformation features indicate that brittle or plastic deformations are very weak or absent in most of the samples and that magmatic deformation is dominant throughout the entire section. This is mostly indicated by very low misorientation angles (Figure 7) and the paucity of petrographic indicators for plastic deformation, such as kink banding or undulose extinction in olivine. The dominance of magmatic deformation implies that the microstructures we observe in our samples can be ascribed to the primary emplacement of crustal material and are not or only weakly affected by any late-stage tectonic process.

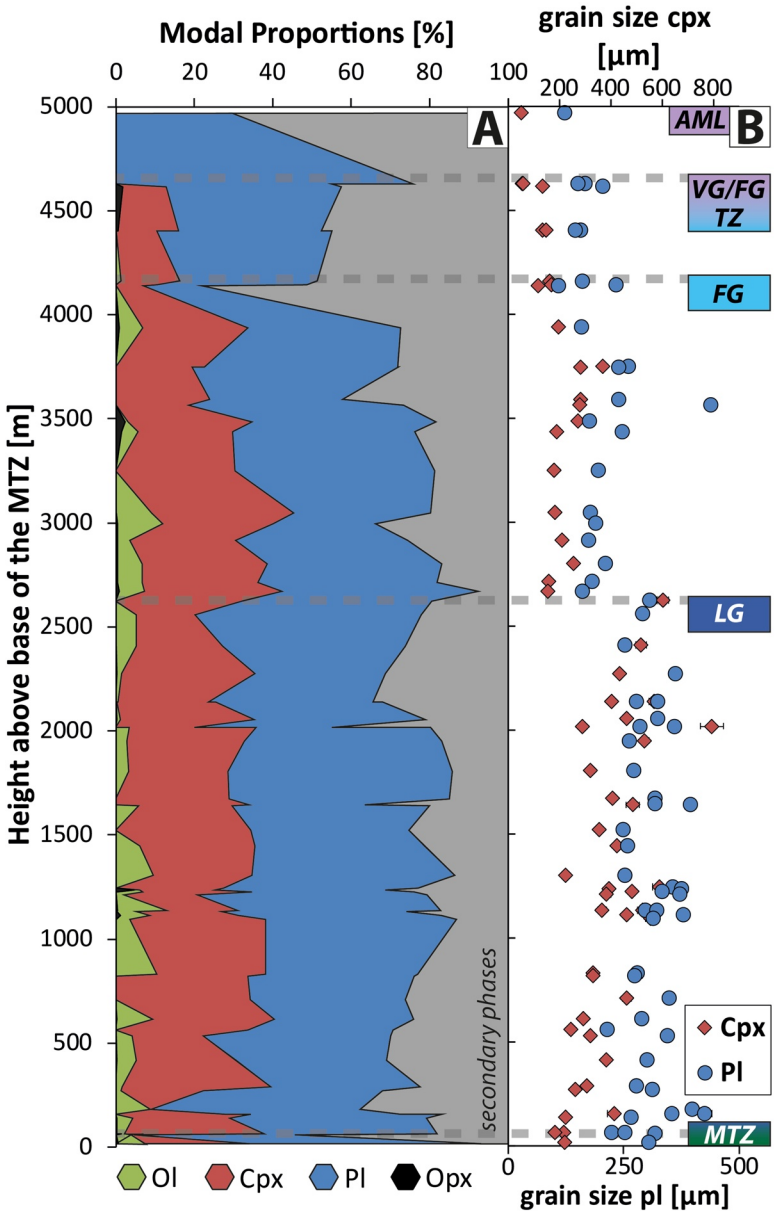

Figure 3. (a) Modal proportions of the phases plagioclase (blue), clinopyroxene (red), olivine (green), orthopyroxene (black), and secondary phases (gray) estimated by EBSD analysis. (b) 2D grain sizes of plagioclase (blue circles) and clinopyroxene (red diamonds); A and B plotted versus height above base of the MTZ. The grain size is plotted as diameter of a circle with the area of the analyzed grain. Black bars give the standard error (smaller than the symbol in most cases). Note different axes for plagioclase and clinopyroxene. Lithological units are given at the right (see text for definition of the abbreviations). Dashed horizontal lines mark transitions between lithological units.

4.2. Crystal Size Distributions

CSD results for plagioclase are shown in Figure 4. They are displayed in a conventional way (Figure 4c) with the population density (n; the number of crystals per volume in a size bin divided by the width of the size bin; Garrido et al., 2001; Marsh, 1988) as a function of the binned crystal size (3D length of the crystals). The CSD plots show linear trends in the mid to large grain sizes and a decreased population density of the finer grains leading to roughly convex upward trends (Figure 4c). Regression lines were calculated using at least three data points and taking a best fit quality of $Q > 0.1$ into account, as suggested by the CSDCorrections software (Higgins, 2000) for an acceptable regression quality. While the linear regression

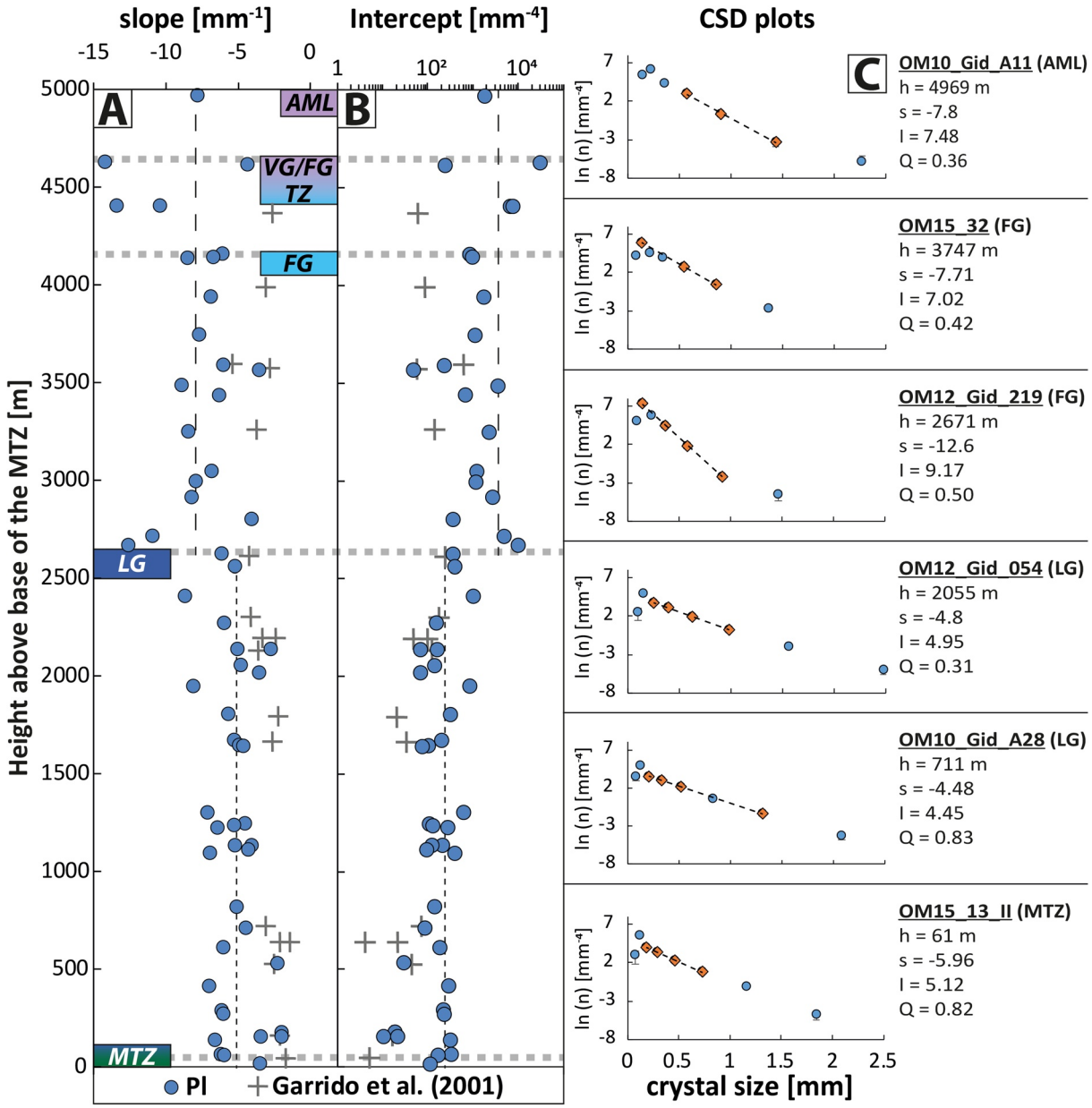

Figure 4. Results of crystal size distribution analysis. Slope (a) and intercept with *y*-axis (b) of the regression line interpolated from at least three data points of the crystal size distribution calculated after Higgins (2000). Blue circles are plagioclase data of this study, red crosses are data from Garrido et al. (2001). Dashed vertical lines give mean from the samples above 2,600, dotted lines below 2,600 m above the Moho (mam). (c) shows representative CSD plots for plagioclase selected for every crustal unit. *y*-axis gives the population density which is the number of crystals per volume divided by the width of the size bin given on the *x*-axis (Marsh, 1988). Orange diamonds are used for calculating the regression line (dashed line). Sample name and corresponding crustal unit are given beside each plot. h, height above base of the MTZ, s, slope, I, *y*-axis intercept, *Q*, quality of the regression given by the CSDCorrections software (Higgins, 2000); $Q_{max} = 1$, $Q > 0.1$ is acceptable. Lithological units are given at the right. Dotted horizontal lines mark transitions between lithological units.

includes the maximum population density at small grain sizes within most of the gabbros of the AML, VG/FG TZ, and FG units, it is restricted to the larger crystal sizes in the LG unit and the MTZ. The slopes of the regression lines as well as their intercept with the *y*-axis were plotted for every sample (Figures 4a and 4b). Marsh (1988) defined the slope of the regression line as measure of the product of overall population growth rate and mean age. The intercept with the *y*-axis is defined as the nucleation density. The slope of the regression line reflects the nucleation rate (steeper slope means faster nucleation) for a constant

growth rate (Marsh, 1988). It provides implications on the cooling rate of the systems since nucleation exponentially increases with faster cooling (e.g., Garrido et al., 2001).

Consistently with the 2D grain sizes obtained by EBSD, both plots show shifts at 2,600 mam toward gentler slopes (Figure 4a) or lower intercepts (Figure 4b). The average slope in the samples from the AML and the FG unit is −7.97; the steepest slope of −14.2 is in the VG/FG TZ unit, and the gentlest slope of −3.54 is in the FG unit. In the LG and MTZ samples, the average slope is −5.14, with the steepest slope of −8.66 in the uppermost LG unit and the gentlest slope of −1.98 in the lowermost LG above the MTZ. The intercept of the regression lines is plotted on a logarithmic scale in order to consider both very low and very high population densities. Its mean is 3,663 mm^{-4} in the units above 2,600 m with a minimum of 47 mm^{-4} in the upper FG unit and a maximum of 29,437 mm^{-4} in the VG/FG TZ unit. In the sections below 2,600 m, the mean of the intercept is 223 mm^{-4} with a minimum of 10.5 mm^{-4} in the lowermost and a maximum of 982 mm^{-4} in the uppermost LG. Maxima of the interception correspond to the lowest (and therefore steepest) slope and vice versa.

4.3. Fabric Strength

The J and M indices show similar trends along the sampled section (Figure 5a). For the sake of simplicity, we describe and discuss the fabric strength using J only. Values of J calculated from average orientation data are slightly lower than those calculated from the pixel data, but show the same relative trends, which we focus on in this study. The depth plots of J for plagioclase and clinopyroxene are given in Figure 5a. With its low number of reliable results, due to the high degree of serpentinization and/or relatively small number of grains, the depth plot of J for olivine is meaningless, and is not presented. Plagioclase data show two distinct trends along the crustal section: the upper part from the dike/gabbro transition at 5,000 mam down to 3,500 mam is characterized by low and relatively stable J, up to 2.1. The second part beneath 3,500 mam shows a stronger scattering, and higher values of J up to 5.1. Because of the significant change in the middle of the FG unit, which is also seen in the symmetry indices (described below), we decided to distinguish the upper foliated gabbros (UFG), where fabric strength is constantly weak, from the lower foliated gabbros (LFG) with increasing and more scattered fabric strengths. J for clinopyroxene shows a similar behavior with relatively stable values <2.5 from the dike/gabbro transition down to about 2,600 mam (Figure 5a). In the LG below 2,600 mam, it is more scattered, and is generally higher, up to 4.84. There is a gentle trend of increasing fabric strength for both plagioclase and clinopyroxene with depth from the top of the LG unit to about 1,000 mam. In the lowermost 1,000 meters, close to the MTZ, the fabric strength of both phases remains more or less constant, and gently decreases in the MTZ samples.

4.4. Pole Figures and Symmetry

Representative pole figures for plagioclase and olivine CPO are shown in Figures 5a and 5c compilation of all pole figures is available in the PANGAEA database (Mock et al., 2020b). The trace of the foliation, corresponding to the preferred orientation of plagioclase (010), is plotted on pole figures of every phase. Plagioclase shows point maxima of (010) along the entire section, mostly correlated with point to girdle distributions of [100]. For quantifying the CPO symmetry, we used BA and BC for plagioclase and clinopyroxene, respectively (Figure 5b). Distinct trends along the crustal section are observed for both phases: the upper 1,500 m of the section are dominated by more or less constant indices with an intermediate symmetry in the section from 5,000 down to 3,500 mam (BA ≈ 0.4 for plagioclase and BC ≈ 0.5 for clinopyroxene). These data indicate that a significant lineation is present within the VG/FG TZ and UFG units as already shown by the pole figures (Figure 5c). At ∼3,000–3,500 mam, a foliation-dominated fabric is represented by a clear minimum of the symmetry indices in both phases (BA = 0.06 for plagioclase and BC = 0.13 for clinopyroxene). Below this horizon, the lineation component gradually becomes stronger down section in both phases, with intermediate to slightly lineated symmetries at the base of the crust with a BA of up to 0.68 for plagioclase and a BC of up to 0.64 for clinopyroxene. Most olivine CPO show [010] point distributions and [001] girdles, or also [001] point maxima. A few of the samples below 1,446 mam have CPO with [100][010] point maxima, parallel to the [100](010) plagioclase CPO (e.g., sample OM15_19AII in Figure 5c).

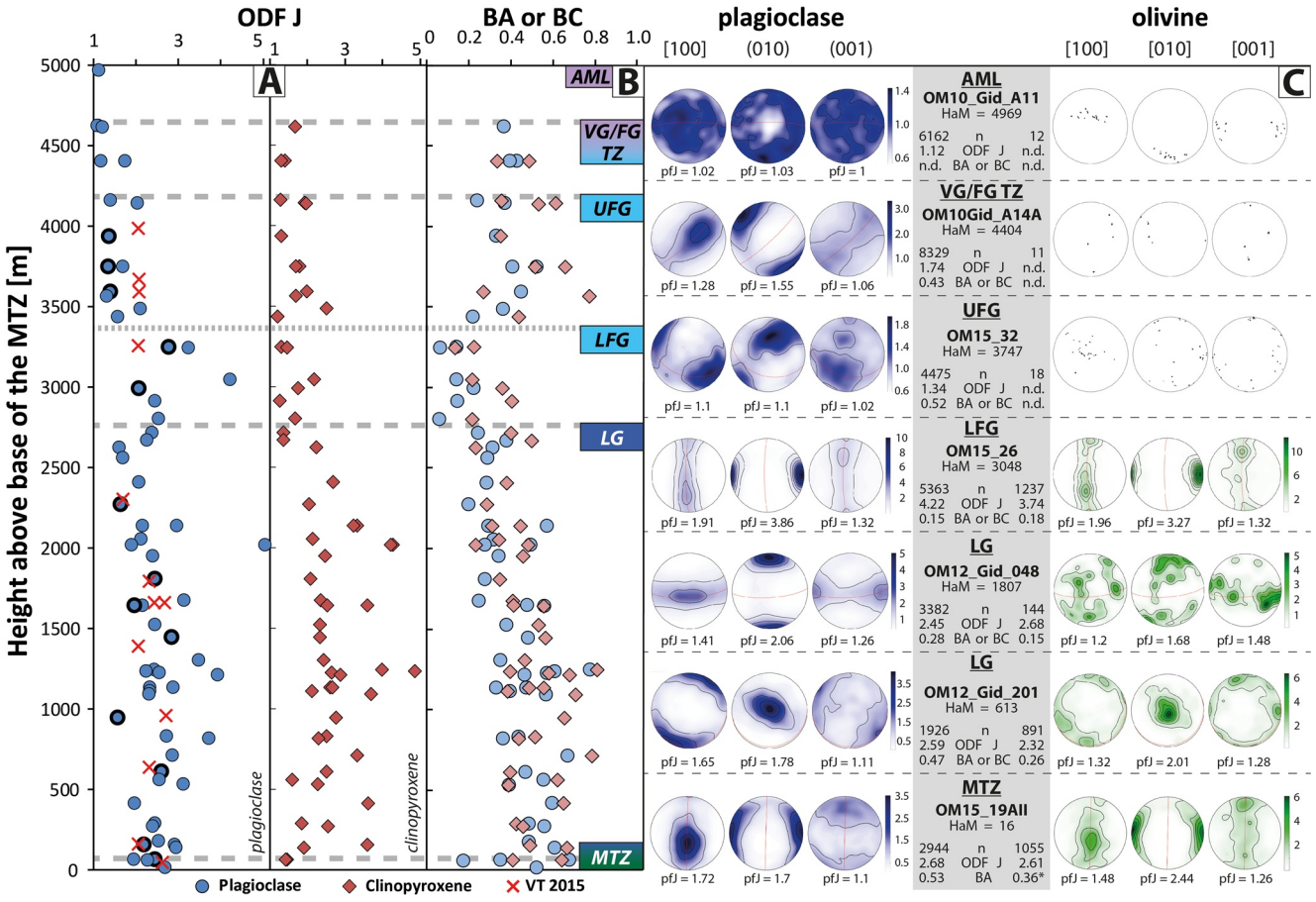

Figure 5. J indices (a) and BA or BC indices (b) of plagioclase and clinopyroxene plotted vs. height above base of the MTZ. Plots show correlating trends with changes at 3,500 m. Blue circles are plagioclase data, red diamonds are clinopyroxene data. Red crosses in (a) are plagioclase data from VanTongeren et al. (2015). Plagioclase data with thicker contours are selected samples close to the stratigraphic height of VanTongeren's data. Their lower spatial resolution conceals a down section trend. Dashed horizontal lines mark transitions between lithological units. (c) pole figures of [100], (010), and (001) of plagioclase (left, blue) and of [100], [010], and [001] of olivine (right, green) arranged by height above base of the MTZ. Representative pole figures for every lithological unit are selected. Sample information are given in the gray box with HaM, Height above the base of the MTZ in meters; n = number of indexed crystals, J, J-index of the orientation distribution function, BA, BA index; BC, BC index; pfJ, J-index of each pole figure (see text for details). Red line represents plagioclase foliation perpendicular to point maximum in (010). Note different color bars. Only the pole figures from samples with more than 100 indexed grains are plotted as contoured figures. n.d. means not determined due to very weak CPO visible in the pole figure. * indicates that we present the BA index for olivine, because the olivine fabric is most pronounced by [100][010] here. We separated the FG unit into upper foliated gabbros (UFG) and lower foliated gabbros (LFG) with respect to significantly differing fabric data; see text for details.

The pole figure J indices (pfJ) of plagioclase and clinopyroxene (Figure 6) plotted versus the crustal height behave similar to J with very low values in the AML, the VG/FG TZ and the UFG unit. In the LFG and LG units, the values are widely scattered. The pfJ of those axes that represent the lineation ([100] in plagioclase, [001] in clinopyroxene) show slight increases down section from 3,500 to 1,000 mam.

4.5. Misorientation

The deformation within grains is quantified using the GOS and GAM (Figures 7a and 7b). Generally, the GOS does not vary much in our sample suite. However, similarly to J, the GOS in plagioclase and clinopyroxene decreases at the transition from the UFG to LFG units and slightly increases down section from 3,500 mam. The GOS in olivine is generally more scattered. It tends to increase down section with maxima of about 1.3° between 1,500 and 1,000 mam. Below 1,000 mam, the olivine GOS decreases to 0.5° at the MTZ. The sample average GOS in both clinopyroxene and plagioclase are relatively constant at about 0.5° from 5,000 down to 3,500 mam where they decrease to 0.3°, and gradually increase down section to 0.8° at 800

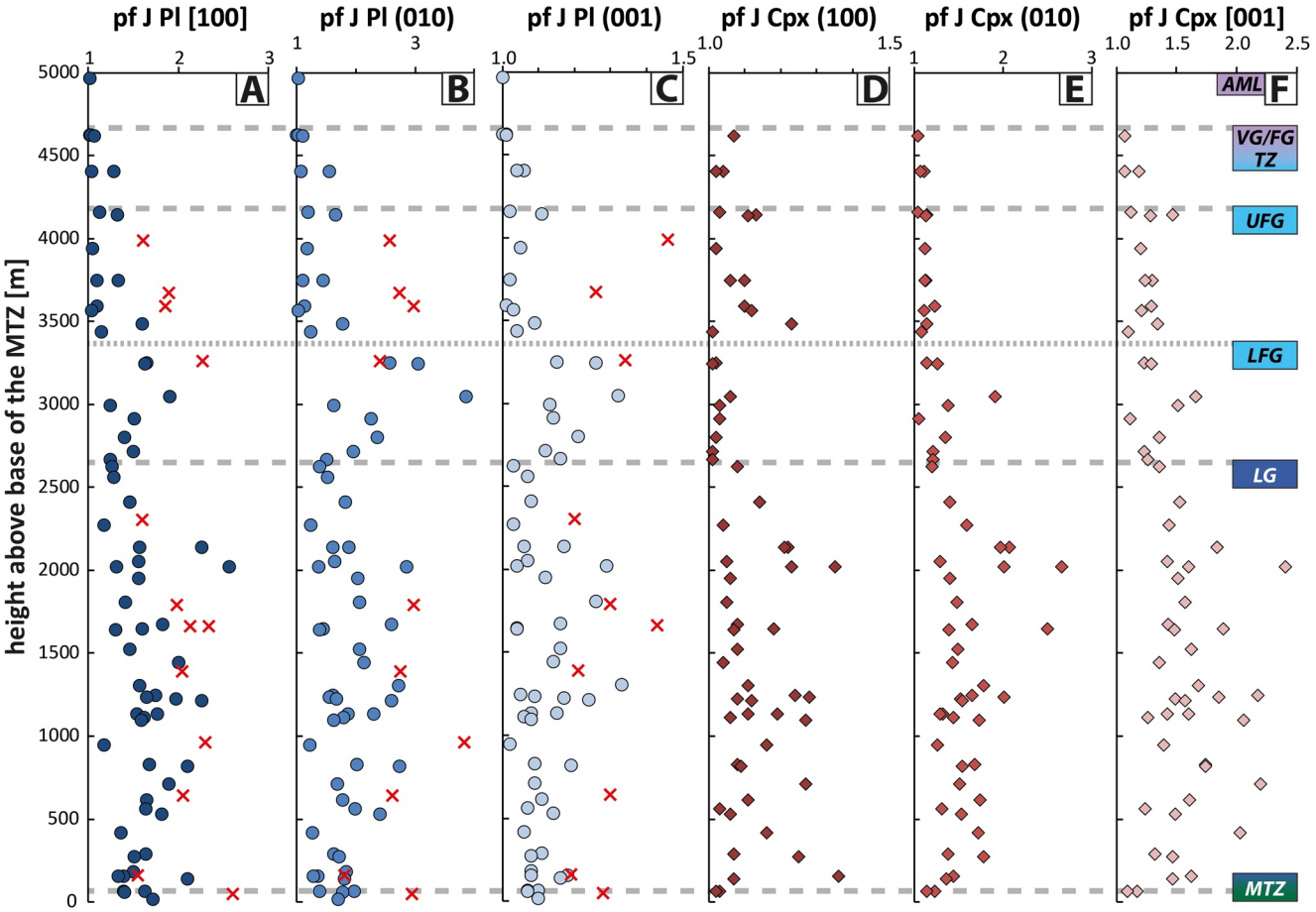

Figure 6. pfJ indices of the three crystallographic axes 100, 010, and 001 of plagioclase (a–c) and clinopyroxene (d–f) plotted versus height above the base of the mantle transition zone (MTZ). Blue circles are plagioclase, red diamonds are clinopyroxene data. Red crosses are plagioclase data from VanTongeren et al. (2015). Lithological units are given at the right. Dashed horizontal lines mark transitions between lithological units. We separated the foliated gabbros (FG) unit into upper foliated gabbros (UFG) and lower foliated gabbros (LFG) with respect to significantly differing fabric data; see text for details.

mam. Below 800 mam, they decrease to 0.5° at the MTZ reproducing the trend observed in olivine. The sample average GAM in all three phases is more scattered than the GOS between 5,000 and 3,500 mam. Similar to the GOS, the GAM increases below 3,500 mam toward a maximum of about 0.7° in olivine and 0.5 or 0.6° in clinopyroxene and plagioclase, respectively. Below 800 mam, the GAM of all phases gradually decreases to about 0.4° at the MTZ. Misorientation in olivine is generally higher than in the other phases. The gradual increase in the LG unit reproduces the increase of J along this section (Figures 5 and 7).

5. Discussion

As summarized in the introduction, apparently contradictory conclusions in several published studies lead to a still on-going debate about the lower fast-spread oceanic crust accretion mechanism(s). Our results obtained in Wadi Gideah provide an opportunity to test the accretion models presented in the introduction in terms of consistency with the microstructural features of the primary phases plagioclase, clinopyroxene and olivine. Magmatic deformation is the most dominant type of deformation in our profile. Low values (≤1°) for the mean angular deviation in all samples emphasize the high data quality, and the relatively high spatial resolution (one sample every 81 m on average) is unique for an entire crustal profile. Compared to previous fabric studies, the high density of our data allows us to identify trends along the crust that were not documented before. This qualifies this section to constrain crustal accretion processes for fast-spreading ridge systems beneath the paleo spreading center that produced the Samail ophiolite. Table 2 provides an

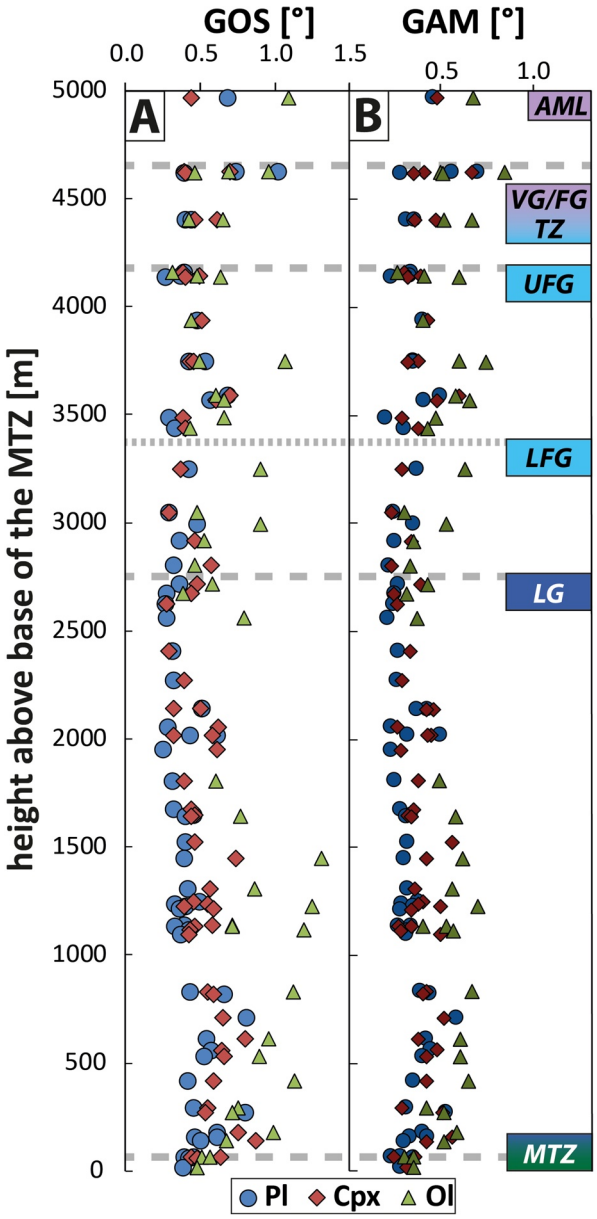

Figure 7. Depth plots of (a) the grain orientation spread (GOS) of plagioclase, clinopyroxene, and olivine representing the degree of intracrystalline deformation averaged per phase and sample and (b) the grain average misorientation (GAM) of plagioclase, clinopyroxene, and olivine representing the intensity of sub-grain formation averaged per phase and sample. Dashed horizontal lines mark transitions between lithological units.

overview of the crustal units we identified in our reference section and compiles microstructural key features and their implications on magmatic processes leading to the emplacement of every unit.

5.1. Re-Evaluating End-Member Accretion Models

Both microstructural features and CSD data show correlated changes within the FG unit between 2,600 and 3,500 mam (Figures 3–7). The changes at 2,600 mam coincide with the transition between the FG and the LG units. Changes at ~3,500 mam are located within the FG unit, separating the UFG unit from the LFG unit. The gabbro glacier model (e.g., Henstock et al., 1993) implies microstructural features that should be observed along the crust as a result of ductile flow. Primary phases are expected in the gabbro glacier model to show a sub-vertical lineation close to the AML gradually rotating to horizontal and Moho-parallel at greater depths. Mineral lineations are described and measured in many field studies in Oman (e.g., Nicolas et al., 2000; Pallister & Hopson, 1981), and were used as an argument supporting a gabbro glacier model (e.g., Quick & Denlinger, 1993). Since the samples in our study were initially taken for geochemical analysis, they are not oriented and we are not able to use thin section orientations to document the global lineation trend at the crustal scale. However, both BA and BC, for pole figures of plagioclase and clinopyroxene, respectively, do not evolve continuously from oblate to prolate symmetry (i.e., from [100] girdles to [100] point maxima in plagioclase) down section as could be expected in a scenario involving ductile flow from the AML (Figure 5b). Instead, BA and BC show significant variations between adjacent samples. A similar conclusion was drawn by VanTongeren et al. (2015) using plagioclase CPO of gabbros from Wadi Khafifah (data points included in Figure 5a). The CPO strength in our study shows an increasing down section trend that may appear consistent with a subsiding crystal mush being transported in a ductile flow. However, the intuitive suggestion that the fabric strength continuously increases within such an environment is questionable. When cumulate mushes from the AML subside, the strength of a fabric does not necessarily depend on the transport distance. As pointed out by Vernon (2000), other parameters like melt fraction, viscosity of the melt and habit of the solids may control if and how strongly the crystals become aligned. Since the mechanical environment and the physical parameters of an assumed subsiding crystal mush may vary along the crust, fabric strength can also be variable along a crustal section with increasing strain. We therefore argue that a critical parameter is not necessarily the fabric strength but its symmetry. The latter varies along the crustal section: lineation is present in the VG/FG TZ and UFG unit, it is weak or even absent in the LFG unit, and increases with strong scattering in the LG unit. This behavior cannot be easily explained by local differences in physical properties of a crystal mush that is deformed by a gabbro glacier at the crustal scale. It rather suggests that the deformation regime changes along the studied profile.

The low J in the AML region, the VG/FG TZ and the UFG unit indicates a random fabric in the samples from the frozen AML to weak CPO showing both foliation and lineation in the samples from the VG/FG TZ and the UFG unit. Müller, Koepke, C. Garbe-Schoenberg, et al. (2017) and Müller, Koepke, C. D. Garbe-Schoenberg, et al. (2017) studied an outcrop representing a frozen AML at the Southern end of Wadi Gideah, where our samples from the AML were taken, and found indicators for multiple sequences of heating and cooling events as well as dynamic vertical movement processes during the lifetime of the AML. They have also reported evidence for the AML intruding into the sheeted dikes at its highest position and

Table 2
Crustal Units With Some Microstructural Key Features

Crustal unit[a]	Upper boundary (interpolated) (mam)[b]	Thickness (m)	General presence of foliation[c]	Which mineral(s) mark the foliation?[d]	General presence of lineation[c]	Which mineral(s) mark the lineation?[d]	Comment	Magmatic process
AML	5010	388	no		No		no fabric	Frozen melt
VG/FG TZ	4622	481	weak	pl, (cpx)	Weak	Pl	1 sample shows only weak foliation and no lineation (sample OM10_Gid_A13)	in part frozen melt lens, in part mush suspension
UFG	4141	616					1 sample shows neither fol nor lin (OM10_Gid_A17_1)	mush suspension
LFG	3525	877	strong	pl, cpx, ol (if present)	No		uppermost (OM15_27) and lowermost (OM12_Gid_219) sample show also weak lineation in pl	more sill intrusions, not affected by mantle convection
LG	2648	2480	strong	pl, (occasionally cpx, ol)	weak-strong	pl, (occasionally cpx, ol)	intensity of lineation increases down section; individual samples fall off this trend (e.g., OM12_Gid_026; OM10_Gid_A26)	sill intrusion, in-situ; increasingly affected by down section
MTZ	168	168	weak-strong	pl, ol, (occasionally cpx)	no-strong	pl, (occasionally cpx, ol)	variable fabrics within the MTZ with differing lineation intensities	sill intrusion, sills with more melt are less affected by mantle convection

Note. See Text for Details
[a]AML, axial melt lens; VG/FG TZ, varitextured gabbro/foliated gabbro transition zone; UFG, upper foliated gabbros; LFG, lower foliated gabbros; LG, layered gabbros; MTZ, mantle transition zone. [b]Crustal height of the upper boundary of every unit in meters above the base of the MTZ (mam). [c]Non-quantitative identifier of the present foliation or lineation with no, weak, strong, or very strong. [d]pl, plagioclase; cpx, clinopyroxene; ol, olivine.

for assimilation of hydrothermally altered roof material during relatively fast cooling of the AML resulting in the formation of the VG unit. France et al. (2009); Müller, Koepke, C. Garbe-Schoenberg, et al. (2017) and Müller, Koepke, C. D. Garbe-Schoenberg, et al. (2017) also showed that the geochemistry of most of the VG unit corresponds to frozen melts rather than to cumulate rocks. This indicates a regime with locally high melt fraction where crystals are free to rotate and previous crystal alignment, if present, is destroyed by melt perturbation or movement (e.g., Vernon, 2000), possibly resulting in the weak fabrics of our samples from the AML and the VG/FG TZ.

If we posit that crystallization of the lower crust occurred only, or at least to a major extent, in the AML, a mechanism is required to explain clear textural differences between the VG/FG TZ and FG units and the LG unit. We observe a substantial and abrupt change from small to coarser grain sizes of plagioclase and clinopyroxene at the transition from the FG to LG units (Figure 3). The smaller grain sizes qualitatively imply a faster cooling of the VG/FG TZ and FG units and a slower cooled LG unit. Although this reflects in principle the findings of Coogan et al. (2002, 2007), who documented by diffusion modeling that the cooling rate decreases down section in the lower crust of the Oman, they described a gradually decreasing trend. Our findings that grain sizes abruptly increase from the LFG to the LG units are similar to the results of Garrido et al. (2001) who studied plagioclase CSD in Wadi Khafifah. The plagioclase CSD in our study calls for a conditional change leading to abruptly smaller crystals above 2,600 mam (Figure 4) and therefore confirms observations by Garrido et al. (2001) who found a significant change in plagioclase grain size at 2,000 mam in Wadi Khafifah. Taking the slight variations in the crustal section thickness in the Wadi Tayin massif into

account (e.g., Nicolas et al., 1996), the change in crystal size can be assumed to occur at a similar relative crustal height. As a general implication, Garrido et al. (2001) concluded that the difference in grain size is due to varying cooling rates along the crust with an abruptly accelerated cooling above 2,000 m (in Wadi Khafifah) compared to the region below. Faster cooling of the uppermost gabbros is also consistent with the interpretation of Nicolas et al. (2009) deduced from gabbros below the root zone of the sheeted dyke complex that these must have been expelled fast through the wall of the AML therefore preserving textures of a fast cooling. Quick and Denlinger (1993) proposed that grain size is inversely related to strain and found that the least strain predicted for uppermost gabbros is consistent with the high textural variety of the rocks near the AML. However, if grain size was inversely related to strain, the increasing strain down section in a subsiding mush should cause a gradual decrease of the grain size. The observed abrupt coarsening of grain sizes at 2,600 mam does not agree with this expectation.

We found that the scenario of a downward ductile flow, inherent in the gabbro glacier model, is consistent with our microstructural data in the uppermost 1,500 m of the gabbroic crust where small, grained textures (Figure 3b) can be explained by an efficient hydrothermal cooling of the AML. Moreover, the observed foliated and lineated fabrics (Figures 5b and 5c), reflecting the possible impact of shearing, are consistent with a downward flow model. This scenario is however not applicable to coarser grained regions below (Figure 3b), which show substantial scattering in the fabric strength, which tends to decrease in the lowermost 1,000 m of the crust (Figure 5a). CPO in the LFG and LG units reflect variable degrees of lineation and foliation at the meter scale along the lower crust, as revealed by the down section plots of BA and BC (Figures 5b and 5c).

MacLeod and Yaouancq (2000), VanTongeren et al. (2015), and Morris et al. (2019) suggested an alternative model for the accretion of the gabbros beneath the AML. They interpret steep foliation in the FG unit of Wadi Abyad (MacLeod & Yaouancq, 2000), Wadi Khafifah (VanTongeren et al., 2015), and wadis Somrah, Khafifah, and Abyad (Morris et al., 2019) as resulting from upward migrating melt aligning the solid phases of the crystal mush. Their model of upward migrating melt is restricted to the FG unit in all sampled sections, where macroscopic foliations in the field are generally steep. Both steep foliations below the AML documented by Pallister and Hopson (1981) or Morales et al. (2011) and our observations from EBSD measurements also agree with this hypothesis in the VG/FG TZ and UFG unit where the pole figures indicate that plagioclase (and to a minor extend also clinopyroxene) fabrics are lineated. This upward flow model is also in agreement with the more efficient cooling of those gabbroic units as indicated by our CSD analyses and also the study of Garrido et al. (2001).

Whereas the uniform subsidence in a gabbro glacier model should result in consistent trends in pole figure symmetry with depth, a down-section trend in a sheeted sill model can be more complex and variable. Crystallization of the gabbros within small melt bodies of variable size and at various depths is not expected to result in clear microstructural or textural trends since small regions crystallize individually and not necessarily in a depth- or time-related sequence (VanTongeren et al., 2015). The relatively low CPO strength of all phases in the gabbros of the AML, VG/FG TZ, and the UFG unit (Figure 5a) could be interpreted as being consistent with the individual crystallization of small melt-rich magma bodies. However, the globally steep foliations in the UFG of the Oman ophiolite (e.g., Macleod & Yaouancq, 2000; Nicolas et al., 2009; Pallister & Hopson, 1981), and observed in Wadi Gideah appear inconsistent with in-situ crystallization of individual sills in the UFG unit. In contrast to the uppermost 1,500 m, the fabric strength in the gabbros below 3,500 mam tends to increase downward, with strong scattering (Figure 5a). Regardless of the observed overall increasing down section trend, the significant variations in fabric strength and pole figure symmetries on a small spatial scale are consistent with individual crystallization of relatively small melt bodies.

Plagioclase pole figures with point maxima in (010) and girdle distributions in [100] in the LFG and upper LG units (i.e., low BA and BC values) indicate a compaction-induced fabric (VanTongeren et al., 2015) where shear, if present, played a minor role. Girdle distributions in [100] pole figures tend to evolve to point maxima down section in the lower LG unit and MTZ (i.e., higher value of BA and BC; Figures 5b and 5c) indicating a stronger lineation, hence likely more significant shearing of the lower crustal regions. Regardless of local variations in CPO strength and pole figure symmetries, a general increase of fabric strength and higher impact of shear strain below 3,500 m was not described in previous CPO studies (e.g., Morales et al., 2011; VanTongeren et al., 2015, Figure 5a). Local differences are well-pronounced for instance in sam-

ples OM12Gid045 and OM12Gid044, which show weaker fabrics, different to those in the samples above and below (see pole figure compilation and microstructural data in Mock et al., 2020b). The differences in J values between earlier fabric studies and our data may be caused by different approaches in the sample selection (i.e., anorthosite in Morales et al., 2011 vs. gabbroic rocks in our study) and/or calculation of the orientation distribution function (see Section 4.1). They do not change the observation that a down section increasing trend in fabric strength is visible along the LG unit in our study. This trend cannot be explained by crystallizing sills alone. A process affecting the CPO strength and symmetry (development of mineral lineation) of all primary phases could be the active flow of the underlying mantle, as proposed based on the continuity of lineation trajectories in the upper mantle and gabbros above, and the inferred mechanical coupling between the mantle and the crystallizing gabbroic mush (Ildefonse et al., 1995; Jousselin et al., 1998, 2012; Nicolas et al., 1994, 2000). In the lower crustal magmatic mush, shear strain imposed by the actively convecting upper mantle can produce a magmatic fabric with a lineation component being most pronounced close to the crust-mantle transition and attenuating up section where the effect of mantle-induced shear is reduced. A limited amount of melt would (a) allow crystal preferred orientation, (b) accommodate the induced shear strain and therefore (c) prevent intracrystalline deformation which would lead to higher misorientation in the grains. Misorientation in the primary phase grains is indeed low, particularly in clinopyroxene and plagioclase, along the entire reference profile (Figure 7). It is generally stronger for olivine than for clinopyroxene or plagioclase (Figure 7), because olivine is more sensitive to crystal-plastic deformation in hypersolidus conditions (Yoshinobu & Hirth, 2002). Decreasing misorientation in the lowermost 800 m of the crust (Figure 7), may relate to a higher melt fraction present in this region when incipient crystal-plastic deformation started to overprint the magmatic fabric. A possible explanation for higher melt proportions in the lowermost 800 m of the crust could be its vicinity to the hot upper mantle or deep melt lenses in the MTZ (e.g., Crawford et al., 1999; Dunn et al., 2000; Garmany, 1989) and correlated emplacement of melt in the MTZ horizon (e.g., Kelemen et al., 1997). Post-magmatic tectonic processes are unlikely to account for the observed misorientation for two main reasons: (a) tectonic emplacement, for example, during obduction, would be expected to affect the entire crust, and not only the LG unit, and (b) if local regions of the crust were affected by plastic strain, for example, in the proximity of fault zones, they might present sharply contrasting misorientation signals. Fault zones have been described in Wadi Gideah (e.g., Zihlmann et al., 2018) indicating that local heterogeneities in plastic deformation intensity might exist. However, the sample suite used in this study did not include samples from fault zones; we therefore assume that the misorientation in our samples is not affected by late plastic deformation.

5.2. Comparison With Previous Fabric Studies in the Samail Ophiolite

The importance of microstructural features to understand magmatic processes during crustal formation led to several studies performed on plutonic rocks from Oman. Nicolas et al. (2009) focused on the root zone of the sheeted dyke complex and the uppermost gabbros and found clear indicators for a crystal mush subsiding from the AML and contributing to the lower crustal accretion. Morales et al. (2011) analyzed anorthosites throughout the uppermost 2,000 m of the gabbros and found an increasing strain down section. Jousselin et al. (2012) investigated microstructures within gabbroic lenses in the MTZ and concluded that the convecting underlying mantle significantly contributes to the deformation of gabbros in the MTZ.

VanTongeren et al. (2015) did not observe any trend in fabric strength along the lower crust in Wadi Khafifah (Figure 5a), which contrasts with the increasing J trend that we observe in the LFG and LG units down to 1,000 mam. We posit that the absence of such a trend in VanTongeren et al. (2015) is possibly an artifact of the lower data density with an average sample spacing of ~330 m. In order to test this hypothesis, we identified 13 data points of our sample suite that are close to the stratigraphic heights of VanTongeren's samples (symbols with thick contours Figure 5a). Indeed, the gaps between the selected data points and the overall distribution conceals a down section trend. This also reveals that the number of samples, hence the data density, significantly affects the measurability of trends. With an average spacing of less than 2 m between adjacent samples of LG cored during the Oman Drilling Project, Mock et al. (2020a) have shown that even on the meter scale gradual changes in plagioclase fabrics occur within the lower oceanic crust. VanTongeren et al. (2015) interpret their plagioclase pole figures as representing no or only very weak lineation by the [100] girdle or weakly clustered distributions. We interpret at least the three samples from the lowermost 1,000 m of the crust in VanTongeren et al. (2015); Figure 4 as revealing a more clustered distribution of [100]

indicating a significant lineation component in the fabric. This interpretation would be consistent with the fabrics we observe in the LG unit of Wadi Gideah, showing stronger lineation with depth as quantified by BA and [100] pfJ increasing along the LFG and LG units. The 14 samples we analyzed in the uppermost 1,500 m of the gabbro section (AML, VG/FG TZ, and UFG) provide a high spatial resolution for a better discussion of accretion models, as suggested by VanTongeren et al. (2015).

Morales et al. (2011) analyzed 15 more or less monomineralic anorthosites mostly from the uppermost 1,500 m of the plutonic crust. The samples correspond to anorthositic layers and lenses of different thickness, which is a significantly different approach to our study using gabbroic samples. Morales et al. (2011) found indicators for increasing strain down section below the root zone of the sheeted dyke complex in the Wadi Tayin massif. This is consistent with the plagioclase [100] point maxima, and relatively high BA we observe along the VG/FG TZ and the UFG units. Although we calculated very low J indices of plagioclase and clinopyroxene in those units (<2.03 for plagioclase, <1.97 for clinopyroxene), Morales et al. found J between 2 and 8.7 increasing down section for steeply foliated and widely scattered J between 2 and 11.9 for flat-lying anorthosites (Figure 8 in Morales et al., 2011). They analyzed anorthosites arguing that they "record the evolution of textures controlled by magmatic flow, compaction and recrystallization more clearly than the enclosing gabbros" (Morales et al., 2011). Magmatic deformation textures might be weaker in our gabbros where mostly three phases of the main crystallization (cotectic crystallization) are present, leading to the observed low J. Moreover, the formation of monomineralic anorthosite crystallized from a cotectic assemblage containing olivine, clinopyroxene and plagioclase, requires a specific sorting process in the context of layer formation, which is not known up to now, increasing the probability that these rocks are not representative of the overall gabbro section.

Nicolas et al. (2009) studied the root zone of the sheeted dyke complex with a focus on the transition from the AML to the gabbroic section. They also found evidence for a gabbro mush subsiding from the floor of the melt lens and contributing to the lower crustal accretion. The random fabrics in the uppermost 10 m below the root zone of the sheeted dyke complex is consistent with the random fabrics we see in the AML samples. They also observe increasing fabric strengths below this horizon, first showing [100] girdles, which then evolve to weak point maxima at 365 m below the root zone of the sheeted dyke complex in a way similar to our results in the VG/FG TZ.

In their microstructural investigation of gabbroic lenses within the MTZ, Jousselin et al. (2012) identified four fabric types depending on the intensity of foliation, lineation or both. We ascribe seven of our samples to the MTZ, between 16 and 157 mam. They also show different fabric symmetries from intermediate (OM15_15D_II) to foliated with a [100] girdle (e.g., OM15_13_II) to foliated and lineated with point maxima in both (010) and [100] (e.g., OM10_Gid_A31). This is consistent with the interpretation of Jousselin et al. (2012) that both compaction and magmatic shearing imposed by the convecting mantle might play a role in creating magmatic deformation of the lowermost gabbros in Oman. Olivine crystals of the lowermost gabbros in our sample suite partially display [100] point maxima, parallel to [100] lineations of plagioclase (Figure 5c). This likely indicates a plastic deformation component recorded by olivine and is consistent with the type 4 layering described by Jousselin et al. (2012) in the MTZ.

5.3. Combining the Evaluated End-Member Processes to a Hybrid Model

Our results point to a hybrid model of lower crustal as explained in the following and depicted in Figure 8. Intermediate pole figure symmetries (BA and BC close to 0.5) along the uppermost 1,500 m of the profile with point maxima in both [100](010) of plagioclase and (010)[001] of clinopyroxene indicate that the rock fabrics are not only foliated but also show significant lineation. Lineation can be explained by either subsiding crystal mush from the AML (e.g., Quick & Denlinger, 1993) or upward migrating porous melt flow (MacLeod & Yaouancq, 2000; Morris et al., 2019; VanTongeren et al., 2015) being dominant in this section. More scattered CPO strengths and significantly distinct pole figure symmetries in the section between 3,500 mam and the MTZ are well-explained by in-situ crystallization of individual magma reservoirs, and do not agree with cumulates being transported by a global flow mechanism from the AML downward. In the horizon between 3,500 and 2,600 mam, both grain size and CPO (J, pfJ, BA, pole figures) significantly change. These changes occur in the same horizon as changes in geochemical and petrolog-

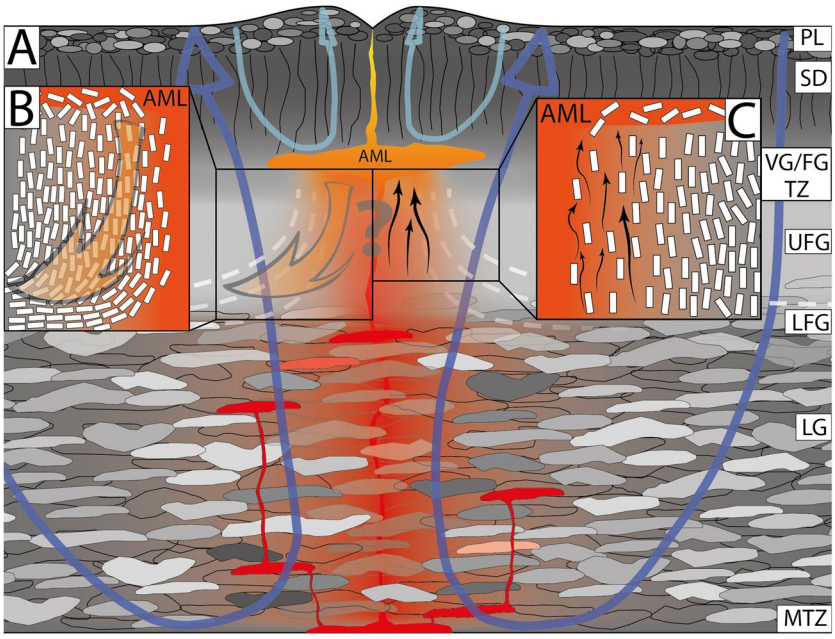

Figure 8. (a) Schematic model of lower crustal accretion beneath fast-spreading mid-ocean ridges based on the results of this study. The data of our study support the crystallization of individual meld bodies (sills) at various depths in the lower oceanic crust (color corresponds to temperature), whereas the data from the varitextured and upper foliated gabbros are in agreement with both a subsiding crystal mush of cumulates from the axial melt lens (orange arrow; see (b) for details) and upward migrating crystal-carrying melt (black arrows and white rectangles; see (c) for details). Both mechanisms may result in the observed steep foliations with significant lineation in the varitextured/foliated gabbro transition and the upper foliated gabbros and agree with our data, symbolized by the question mark. See text for further discussion. Blue arrows represent hydrothermal activity (light blue for the shallow, and dark blue for the deep crust), the curved, dashed lines symbolize the foliations observed in the field.

ical data from the same sample suite do (Garbe-Schönberg et al., 2014; Koepke et al., 2017; Müller, 2016; Müller, Koepke, C. Garbe-Schoenberg, et al., 2017; Müller, Koepke, C. D. Garbe-Schoenberg, et al., 2017; Müller et al., 2014). We interpret them as indicators for changing formation mechanisms, calling for a hybrid crustal accretion model that combines in-situ crystallizing melt bodies in the LFG unit and the LG unit with flow-dominated transport of crystals in the UFG unit and VG/FG TZ. A two-mechanisms accretion model is consistent with the sheeted sill model of Kelemen et al. (1997), which posits that the uppermost horizon beneath the AML might form by subsiding mushes from the AML. However, we infer from previous studies (Garrido et al., 2001; Kelemen et al., 1997; Korenaga & Kelemen, 1997; VanTongeren et al., 2015) supporting a sheeted sill model that this horizon is relatively thin expanding over only a few hundred meters below the AML. Our results suggest that a change in the accretion mechanism occurred ~1,500 m below the AML indicating that the lower two thirds of the analyzed section crystallized at depth whereas the upper third results either from subsiding mush from the AML or from upward migrating porous melt flow. We therefore suggest to describe crustal accretion by a hybrid model where several accretion mechanisms play key roles, rather than by the end-member sheeted sill (e.g., Kelemen et al., 1997) or gabbro glacier (e.g., Henstock et al., 1993) models. Boudier et al. (1996) already proposed a hybrid accretion model where sill intrusions crystallize randomly distributed within a gabbro glacier that expands over the entire lower crust. The gabbro glacier mechanism is restricted in our model to the upper 1,500 m of the lower crust leading to a clear spatial separation between in-situ crystallization within the lowermost 3,500 m and vertical crystal mush movement in the uppermost 1,500 m of the lower crust. This is a key difference between our model and the hybrid model of Boudier et al. (1996). Increasing CPO strength accompanied by slightly higher misorientation in the LG unit can be caused by mantle flow-induced deformation (Jousselin et al., 2012; Nicolas et al., 1994) in the presence of a limited amount of melt. This (likely syn-magmatic) secondary process is compatible with magma reservoirs crystallizing deep in the crust. The weak lineation component in plagioclase and clinopyroxene (low BA or BC, respectively) within the

LFG unit could then result from the less pronounced effect of shear strain forced by mantle flow higher up in the section. Shear strain induced by the upper mantle flow is also consistent with lineated [100][010] olivine CPO that match the [100](010) lineation of plagioclase as described above. This feature indicates plastically deformed olivine in those samples (Jousselin et al., 2012), as well as increasing GOS and GAM in olivine (Figure 7).

Assuming that the UFG unit started to crystallize within the AML, efficient cooling of this horizon by seawater circulation within the sheeted dike complex can explain the small grain size of the UFG unit. An off-axis hydrothermal cooling system, as suggested by Garrido et al. (2001), reaching the FG unit could alternatively explain finer grain sizes from this region in a scenario of upward migrating magma crystallizing beneath the AML. To form the coarser grained LG unit, a different crystallization regime is required. Individually crystallizing magma reservoirs are consistent with scattering of the microstructural parameters and the observed differences between several adjacent samples (Table 1; e.g., from OM12_Gid_026 at 1,246 mam to OM12_Gid_027 at 1,237 mam, or from OM11_Gid_A26 at 945 mam to OM11_Gid_A27 at 831 mam). A requirement for in-situ crystallization is a hydrothermal cooling system removing the latent heat of crystallization. The petrological record in gabbros from high-temperature fault zones in the Wadi Gideah implies that such a system indeed exists (Koepke et al., 2014). Although several authors describe hydrothermal activity in the lower crust of the Samail ophiolite (e.g., Abily et al., 2011; Bosch et al., 2004; Zihlmann et al., 2018), cooling of these units may be less efficient and slower than within the overlying units (e.g., Coogan et al., 2002, 2007; Garrido et al., 2001) resulting in coarser grain sizes of the primary phases. However, this is contradictory to the quantitative cooling results of VanTongeren et al. (2008) who calculated cooling rates using Ca in olivine without significant trends down section, or to the fast cooling along the crust numerically modeled by Hasenclever et al. (2014). We point out that our interpretation from plagioclase CSD that cooling is slower in the LG unit than in the FG unit and the FG/VG TZ is only qualitative. We therefore do not speculate here whether the cooling of the lowermost crust is sufficient to enable in-situ crystallization. Nonetheless, we wish to emphasize that from a microstructural point of view, magma reservoirs crystallizing at depth provide a plausible explanation for the observed trends and variabilities in fabric strength and symmetry.

6. Conclusions

We sampled a cross section along the Wadi Gideah in the Wadi Tayin massif of the Samail ophiolite in order to establish a reference profile through the lower crust from the AML down to the MTZ. Wadi Gideah provides an ideal opportunity for this, since all primary lithological units of the gabbroic crust (VG/FG TZ, FG, LG, and MTZ) are present and observable in surface outcrops. Our results show that the VG and the UFG units (above 3,500 mam) and LFG and the LG units (below 3,500 mam) accreted either in different deformation regimes or by different processes or both, as indicated by differences in textural features and differences in the characteristics of CPO above and below 3,500 mam. A constantly weak CPO with moderate lineation in the VG/FG TZ and the UFG unit contrasts with stronger variations in the LFG and LG units. This variability is consistent with small-scaled magmatic systems crystallizing individually at various times and depths whereas the former indicate a formation mechanism aligning formerly crystallized phases. We found that our data are in good agreement with a hybrid accretion model where the UFG and VG are either accumulated in the AML and subsiding downward (e.g., Quick & Denlinger, 1993) or crystallized from an upward migrating crystal-laden magma (e.g., MacLeod & Yaouancq, 2000). In our hybrid model, the LFG and LG units formed by multiple sill intrusions (e.g., Kelemen et al., 1997). This hybrid model is generally consistent with the sheeted sill model proposed by Kelemen et al. (1997), where the gabbros directly beneath the AML are also formed by subsiding crystal mush. However, our data indicate a thicker portion of the upper gabbros being built by subsidence and/or upward melt migration. The LFG unit between 3,500 and 2,600 mam could represent a transition zone between the two mechanisms. The increasingly lineated fabric from the top of the LFG unit down section, together with a consistent trend of slightly increasing fabric strength, is consistent with shear deformation induced by mantle flow.

Data Availability Statement

The data obtained for this study and discussed in this study are available on the FAIR-aligned pangaea repository under https://doi.org/10.1594/PANGAEA.924445.

Acknowledgments
The authors wish to thank J. Feige, C. Nevado, and D. Delmas for careful thin section preparation. F. Barou is acknowledged for helpful assistance during EBSD measurements. The authors thank Maël Allard and David Mainprice for their help with MTEX. We acknowledge Michael Denis Higgins for providing the CSDCorrections 1.60 software we used to calculate crystal size distributions. The support of the Sultan Qaboos University (Prof. Sobhi Nasir), as well as the friendly cooperation established in Oman with the Public Authority for Mining (Department of Geological Research, Dr. A. Al Rajhi, Dr. M. Al-Battashi, Dr. M. Alaraimi) are acknowledged. The submitted version of the paper improved by the helpful revisions of David Jousselin, Jill VanTongeren, an anonymous reviewer and the associate editor. This study was funded by DFG projects KO 1723/16-1, KO 1723/21-1, and KO 1723/25-1. Open access funding enabled and organized by Projekt DEAL.

References

Abily, B., Ceuleneer, G., & Launeau, P. (2011). Synmagmatic normal faulting in the lower oceanic crust: Evidence from the Oman ophiolite. *Geology*, *39*(4), 391–394. https://doi.org/10.1130/g31652.1

Anonymous. (1972). Penrose field conference: Ophiolites. *Geotimes*, *17*, 24–25.

Bachmann, F., Hielscher, R., & Schaeben, H. (2010). Texture analysis with MTEX-free and open source software toolbox. Paper presented at the *Solid State Phenomena*. Trans Tech Publications Ltd.

Boddupalli, B., & Canales, J. P. (2019). Distribution of crustal melt bodies at the hot spot-influenced section of the Galápagos spreading centre from seismic reflection images. *Geophysical Research Letters*, *46*(9), 4664–4673. https://doi.org/10.1029/2019gl082201

Bosch, D., Jamais, M., Boudier, F., Nicolas, A., Dautria, J.-M., & Agrinier, P. (2004). Deep and high-temperature hydrothermal circulation in the Oman ophiolite—Petrological and isotopic evidence. *Journal of Petrology*, *45*, 1181–1208. https://doi.org/10.1093/petrology/egh010

Boudier, F., Nicolas, A., & Ildefonse, B. (1996). Magma chambers in the Oman ophiolite: Fed from the top and the bottom. *Earth and Planetary Science Letters*, *144*(1–2), 239–250. https://doi.org/10.1016/0012-821x(96)00167-7

Bown, J. W., & White, R. S. (1994). Variation with spreading rate of oceanic crustal thickness and geochemistry. *Earth and Planetary Science Letters*, *121*(3–4), 435–449. https://doi.org/10.1016/0012-821x(94)90082-5

Brown, T., Cheadle, M., John, B., Coogan, L., Gee, J., Karson, J. A., & Swapp, S. (2019). Textural character of gabbroic rocks from pito deep: A record of magmatic processes and the genesis of the upper plutonic crust at fast-spreading mid-ocean ridges. *Journal of Petrology*, *60*(5), 997–1026. https://doi.org/10.1093/petrology/egz022

Browning, P. (1984). Cryptic variation within the cumulate sequence of the Oman ophiolite: Magma chamber depth and petrological implications. *Geological Society, London, Special Publications*, *13*(1), 71–82. https://doi.org/10.1144/gsl.Sp.1984.013.01.07

Bunge, H. J., & Bunge, H. (1982). *Texture analysis in materials science: Mathematical methods*. Buttleworth.

Canales, J. P., Nedimovic, M. R., Kent, G. M., Carbotte, S. M., & Detrick, R. S. (2009). Seismic reflection images of a near-axis melt sill within the lower crust at the Juan de Fuca ridge. *Nature*, *460*(7251), 89–93. https://doi.org/10.1038/nature08095

Cann, J. R. (1974). Model for oceanic crustal structure developed. *Geophysical Journal of the Royal Astronomical Society*, *39*(1), 169–187. https://doi.org/10.1111/j.1365-246X.1974.tb05446.x

Cannat, M., Manatschal, G., Sauter, D., & Peron-Pinvidic, G. (2009). Assessing the conditions of continental breakup at magma-poor rifted margins: What can we learn from slow spreading mid-ocean ridges? *Comptes Rendus Geoscience*, *341*(5), 406–427. https://doi.org/10.1016/j.crte.2009.01.005

Caress, D. W., Burnett, M. S., & Orcutt, J. A. (1992). Tomographic image of the axial low-velocity zone at 12° 50′ N on the East Pacific Rise. *Journal of Geophysical Research*, *97*(B6), 9243–9263. https://doi.org/10.1029/92jb00287

Chen, Y. J. (1992). Oceanic crustal thickness versus spreading rate. *Geophysical Research Letters*, *19*(8), 753–756. https://doi.org/10.1029/92gl00161

Coogan, L. A., Jenkin, G. R. T., & Wilson, R. N. (2002). Constraining the cooling rate of the lower oceanic crust: A new approach applied to the Oman ophiolite. *Earth and Planetary Science Letters*, *199*(1–2), 127–146. https://doi.org/10.1016/s0012-821x(02)00554-x

Coogan, L. A., Jenkin, G. R. T., & Wilson, R. N. (2007). Contrasting cooling rates in the lower oceanic crust at fast- and slow-spreading ridges revealed by geospeedometry. *Journal of Petrology*, *48*(11), 2211–2231. https://doi.org/10.1093/petrology/egm057

Crawford, W. C., Webb, S. C., & Hildebrand, J. A. (1999). Constraints on melt in the lower crust and Moho at the East Pacific Rise, 9 48′ N, using seafloor compliance measurements. *Journal of Geophysical Research*, *104*(B2), 2923–2939.

Detrick, R. S., Buhl, P., Vera, E., Mutter, J., Orcutt, J., Madsen, J., & Brocher, T. (1987). Multichannel seismic imaging of a crustal magma chamber along the East Pacific Rise. *Nature*, *326*, 35–41. https://doi.org/10.1038/326035a0

Dick, H. J. B., Lin, J., & Schouten, H. (2003). An ultraslow-spreading class of ocean ridge. *Nature*, *426*(6965), 405–412. https://doi.org/10.1038/nature02128

Dunn, R. A., Toomey, D. R., & Solomon, S. C. (2000). Three-dimensional seismic structure and physical properties of the crust and shallow mantle beneath the East Pacific Rise at 9 degrees 30′N. *Journal of Geophysical Research*, *105*(B10), 23537–23555. https://doi.org/10.1029/2000jb900210

Faak, K., Coogan, L. A., & Chakraborty, S. (2015). Near conductive cooling rates in the upper-plutonic section of crust formed at the East Pacific Rise. *Earth and Planetary Science Letters*, *423*, 36–47. https://doi.org/10.1016/j.epsl.2015.04.025

France, L., Ildefonse, B., & Koepke, J. (2009). Interactions between magma and the hydrothermal system in the Oman ophiolite and in IODP hole 1256D: Fossilisation of a dynamic melt lens at fast spreading ridges. *Geochemistry, Geophysics, Geosystems*, *10*, Q10O19. https://doi.org/10.1029/2009GC002652

Garbe-Schoenberg, C.-D., Koepke, J., Mueller, T., Wolff, P. E., & Strauss, H. (2014). Trace element systematics in the plutonic section of fast-spread oceanic crust-evidence from the Wadi Gideah reference profile (Wadi Tayin Massif, Oman ophiolite). In *AGU Fall Meeting Abstracts* (Vol. 2014, pp. V31B-4728).

Garmany, J. (1989). Accumulations of melt at the base of young oceanic crust. *Nature*, *340*(6235), 628–632. https://doi.org/10.1038/340628a0

Garrido, C. J., Kelemen, P. B., & Hirth, G. (2001). Variation of cooling rate with depth in lower crust formed at an oceanic spreading ridge: Plagioclase crystal size distributions in gabbros from the Oman ophiolite. *Geochemistry, Geophysics, Geosystems*, *2*, 2000GC000136. https://doi.org/10.1029/2000gc000136

Gillis, K. M., Snow, J., Klaus, A., Guerin, G., Abe, N., Akizawa, N., et al. (2014). Expedition 345 summary. Paper presented at the *Proceedings of the Integrated Ocean Drilling Program*.

Gillis, K. M., Snow, J. E., Klaus, A., Abe, N., Adriao, A. B., Akizawa, N., et al. (2014). Primitive layered gabbros from fast-spreading lower oceanic crust. *Nature*, *505*(7482), 204–207. https://doi.org/10.1038/nature12778

Goodenough, K. M., Thomas, R. J., Styles, M. T., Schofield, D. I., & MacLeod, C. J. (2014). Records of ocean growth and destruction in the Oman-UAE ophiolite. *Elements*, *10*(2), 109–114. https://doi.org/10.2113/gselements.10.2.109

Hale, L. D., Morton, C. J., & Sleep, N. H. (1982). Reinterpretation of seismic reflection data over the East Pacific Rise. *Journal of Geophysical Research*, *87*(B9), 7707–7717. https://doi.org/10.1029/jb087ib09p07707

Harding, A., Orcutt, J., Kappus, M., Vera, E., Mutter, J., Buhl, P., et al. (1989). Structure of young oceanic crust at 13 N on the East Pacific Rise from expanding spread profiles. *Journal of Geophysical Research*, *94*(B9), 12163–12196. https://doi.org/10.1029/jb094ib09p12163
Hasenclever, J., Theissen-Krah, S., Rupke, L. H., Morgan, J. P., Iyer, K., Petersen, S., & Devey, C. W. (2014). Hybrid shallow on-axis and deep off-axis hydrothermal circulation at fast-spreading ridges. *Nature*, *508*(7497), 508–512. https://doi.org/10.1038/nature13174
Henstock, T. J., Woods, A. W., & White, R. S. (1993). The accretion of oceanic crust by episodic sill intrusion. *Journal of Geophysical Research: Solid Earth*, *98*(B3), 4143–4161. https://doi.org/10.1029/92jb02661
Herron, T. J., Stoffa, P. L., & Buhl, P. (1980). Magma chamber and mantle reflections-East Pacific Rise. *Geophysical Research Letters*, *7*(11), 989–992. https://doi.org/10.1029/gl007i011p00989
Hielscher, R., & Schaeben, H. (2008). A novel pole figure inversion method: Specification of the MTEX algorithm. *Journal of Applied Crystallography*, *41*(6), 1024–1037. https://doi.org/10.1107/s0021889808030112
Higgins, M. D. (1994). Numerical modeling of crystal shapes in thin sections: Estimation of crystal habit and true size. *American Mineralogist*, *79*(1–2), 113–119.
Higgins, M. D. (2000). Measurement of crystal size distributions. *American Mineralogist*, *85*(9), 1105–1116. https://doi.org/10.2138/am-2000-8-901
Ildefonse, B., Abe, N., Blackman, D. K., Canales, J. P., Isozaki, Y., Kodaira, S., et al. (2010). The MoHole: A crustal journey and mantle quest, workshop in Kanazawa, Japan, 3–5 June 2010. *Scientific Drilling*, *10*, 56–63. https://doi.org/10.5194/sd-10-56-2010
Ildefonse, B., Abe, N., Godard, M., Morris, A., Teagle, D. A., & Umino, S. (2014). Formation and evolution of oceanic lithosphere: New insights on crustal structure and igneous geochemistry from ODP/IODP Sites 1256, U1309, and U1415. In *Developments in Marine Geology* (Vol. 7, pp. 449–505). Elsevier. https://doi.org/10.1016/b978-0-444-62617-2.00017-7
Ildefonse, B., Billiau, S., & Nicolas, A. (1995). A detailed study of mantle flow away from diapirs in the Oman ophiolite. In *Mantle and lower crust exposed in oceanic ridges and in ophiolites*, (pp. 163–177). Springer. https://doi.org/10.1007/978-94-015-8585-9_7
Ismaıl, W. B., & Mainprice, D. (1998). An olivine fabric database: An overview of upper mantle fabrics and seismic anisotropy. *Tectonophysics*, *296*(1-2), 145–157.
Jousselin, D., Morales, L. F. G., Nicolle, M., & Stephant, A. (2012). Gabbro layering induced by simple shear in the Oman ophiolite Moho transition zone. *Earth and Planetary Science Letters*, *331–332*, 55–66. https://doi.org/10.1016/j.epsl.2012.02.022
Jousselin, D., Nicolas, A., & Boudier, F. (1998). Detailed mapping of a mantle diapir below a paleo-spreading center in the Oman ophiolite. *Journal of Geophysical Research*, *103*(B8), 18153–18170. https://doi.org/10.1029/98jb01493
Karson, J. A., Kelley, D. S., Fornari, D. J., Perfit, M. R., & Shank, T. M. (2015). *Discovering the deep: A photographic atlas of the seafloor and ocean crust*. Cambridge University Press.
Kelemen, P. B., & Aharanov, E. (1998). Periodic formation of magma fractures and generation of layered gabbros in the lower crust beneath oceanic spreading ridges. *Geophysical Monograph-American Geophysical Union*, *106*, 267–290.
Kelemen, P. B., Koga, K., & Shimizu, N. (1997). Geochemistry of gabbro sills in the crust-mantle transition zone of the Oman ophiolite: Implications for the origin of the oceanic lower crust. *Earth and Planetary Science Letters*, *146*(3–4), 475–488. https://doi.org/10.1016/s0012-821x(96)00235-x
Kelemen, P. B., Matter, J. M., Teagle, D. A. H., Coggon, J. A., & the Oman Drilling Project Science Team. (2020). *Proceedings of the Oman drilling project*: College Station, TX. International Ocean Discovery Program. https://doi.org/10.14379/OmanDP.proc.2020
Koepke, J., France, L., Müller, T., Faure, F., Goetze, N., Dziony, W., & Ildefonse, B. (2011). Gabbros from IODP Site 1256, equatorial Pacific: Insight into axial magma chamber processes at fast spreading ocean ridges. *Geochemistry, Geophysics, Geosystems*, *12*(9), Q09014. https://doi.org/10.1029/2011gc003655
Koepke, J., Garbe-Schoenberg, D., Mueller, T., Mueller, M., Mock, D., Strauss, H., et al. (2017). A Reference Section through the Lower Fast-spreading oceanic crust in the Wadi Gideah (Sumail ophiolite, Sultanate Oman): Drill Sites GT1A and GT2A within the ICDP Oman Drilling Project. Paper presented at *2017 Fall Meeting, AGU*, New Orleans.
Koepke, J., Mueller, T., Linsler, S., Schuth, S., Garbe-Schoenberg, D., & McCaig, A. M. (2014). Invasion of seawater-derived fluids at very high temperatures in the Oman Ophiolite—A key for cooling the deep crust at fast-spreading ridges. Paper presented at *2014 Fall Meeting, AGU*.
Korenaga, J., & Kelemen, P. B. (1997). Origin of gabbro sills in the Moho transition zone of the Oman ophiolite: Implications for magma transport in the oceanic lower crust. *Journal of Geophysical Research*, *102*(B12), 27729–27749. https://doi.org/10.1029/97jb02604
Maclennan, J., Hulme, T., & Singh, S. C. (2005). Cooling of the lower oceanic crust. *Geology*, *33*, 357–360. https://doi.org/10.1130/g21207.1
MacLeod, C. J., & Yaouancq, G. (2000). A fossil melt lens in the Oman ophiolite: Implications for magma chamber processes at fast spreading ridges. *Earth and Planetary Sciences Letters*, *176*, 357–373. https://doi.org/10.1016/s0012-821x(00)00020-0
Mainprice, D., Bachmann, F., Hielscher, R., & Schaeben, H. (2015). Descriptive tools for the analysis of texture projects with large datasets using MTEX: Strength, symmetry and components. *Geological Society, London, Special Publications*, *409*(1), 251–271. https://doi.org/10.1144/sp409.8
Mainprice, D., & Silver, P. G. (1993). Interpretation of SKS-waves using samples from the subcontinental lithosphere. *Physics of the Earth and Planetary Interiors*, *78*(3–4), 257–280. https://doi.org/10.1016/0031-9201(93)90160-b
Marjanovic, M., Carbotte, S. M., Carton, H., Nedimovic, M. R., Mutter, J. C., & Canales, J. P. (2014). A multi-sill magma plumbing system beneath the axis of the East Pacific Rise. *Nature Geoscience*, *7*(11), 825–829. https://doi.org/10.1038/ngeo2272
Marjanovic, M., Carton, H., Carbotte, S. M., Nedimović, M. R., Mutter, J. C., & Canales, J. P. (2015). Distribution of melt along the East Pacific Rise from 9°30′ to 10°N from an amplitude variation with angle of incidence (AVA) technique. *Geophysical Journal International*, *203*(1), 1–21. https://doi.org/10.1093/gji/ggv251
Marsh, B. D. (1988). Crystal size distribution (CSD) in rocks and the kinetics and dynamics of crystallization. *Contributions to Mineralogy and Petrology*, *99*(3), 277–291. https://doi.org/10.1007/bf00375362
Mock, D., Ildefonse, B., Müller, T., & Koepke, J. (2020a) Crystallographic preferred orientations in Wadi Gideah (Oman)-refining a reference profile along lower oceanic crust. Paper presented at the *AGU Fall Meeting 2020*.
Mock, D., Ildefonse, B., Müller, T., & Koepke, J. (2020b). *Electron Backscatter Diffraction (EBSD) analysis through fast-spread lower oceanic crust of Wadi Gideah in the Oman ophiolite*. PANGAEA. https://doi.org/10.1594/PANGAEA.924445
Mock, D., Neave, D., Müller, S., Garbe-Schönberg, D., Namur, O., Ildefonse, B., & Koepke, J. (2020). Formation of igneous layering in the lower oceanic crust from the Samail Ophiolite, Sultanate of Oman. *Journal of Geophysical Research: Solid Earth*. *126*, e2020JB019573.
Morales, L. F. G., Boudier, F., & Nicolas, A. (2011). Microstructures and crystallographic preferred orientation of anorthosites from Oman ophiolite and the dynamics of melt lenses. *Tectonics*, *30*(2), TC2011. https://doi.org/10.1029/2010tc002697
Morris, A., Meyer, M., Anderson, M. W., & MacLeod, C. J. (2019). What do variable magnetic fabrics in gabbros of the Oman ophiolite reveal about lower oceanic crustal magmatism at fast spreading ridges? *Geology*, *47*(3), 275–278. https://doi.org/10.1130/g45442.1

Morton, J. L., & Sleep, N. H. (1985). Seismic reflections from a Lau basin magma chamber. *Geology and Offshore Resources of Pacific Island Arcs-Tonga Region*, *2*, 451–453.

Müller, S., Koepke, J., Garbe-Schoenberg, C., Müller, T., Mock, D., Strauss, H., et al. (2017). A Reference Section through the Lower Fast-spreading Oceanic Crust in the Wadi Gideah (Sumail ophiolite, Sultanate Oman): Drill Sites GT1A and GT2A within the ICDP Oman Drilling Project. In *AGU Fall Meeting Abstracts* (Vol. 2017, pp. V43G-2957).

Müller, T. (2016). *A petrological and geochemical cross section of lower crust at the Wadi Gideah (Samail ophiolite): Implications for the crustal accretion at fast-spreading mid-ocean ridges. Implications for the crustal accretion at fast-spreading mid-ocean ridges. (PhD thesis)*. University of Hannover.

Müller, T., Koepke, J., Garbe-Schonberg, C. D., Dietrich, M., Bauer, U., & Wolff, P. B. (2017). Anatomy of a frozen axial melt lens from a fast-spreading paleo-ridge (Wadi Gideah, Oman ophiolite). *Lithos*, *272*, 31–45. https://doi.org/10.1016/j.lithos.2016.11.022

Müller, T., Koepke, J., Garbe-Schoenberg, C.-D., Schuth, S., & Wolff, P. E. (2014). Oman ophiolite: Petrological and geochemical investigation of fast-spreading crust formation processes. In *AGU Fall Meeting Abstracts* (Vol. 2014, pp. V31B-4727).

Nicolas, A. (1989). *Structures of ophiolites and dynamics of oceanic lithosphere*. Kluwer.

Nicolas, A., Boudier, F., & France, L. (2009). Subsidence in magma chamber and the development of magmatic foliation in Oman ophiolite gabbros. *Earth and Planetary Science Letters*, *284*(1), 76–87. https://doi.org/10.1016/j.epsl.2009.04.012

Nicolas, A., Boudier, F., & Ildefonse, B. (1994). Evidence from the Oman ophiolite for active mantle upwelling beneath a fast-spreading ridge. *Nature*, *370*(6484), 51–53. https://doi.org/10.1038/370051a0

Nicolas, A., Boudier, F., & Ildefonse, B. (1996). Variable crustal thickness in the Oman ophiolite: Implication for oceanic crust. *Journal of Geophysical Research*, *101*(B8), 17941–17950. https://doi.org/10.1029/96jb00195

Nicolas, A., Boudier, F., Ildefonse, B., & Ball, E. (2000). Accretion of Oman and United Arab Emirates ophiolite-discussion of a new structural map. *Marine Geophysical Researches*, *21*(3–4), 147–179. https://doi.org/10.1023/a:1026769727917

Nicolas, A., Reuber, I., & Benn, K. (1988). A new magma chamber model based on structural studies in the Oman ophiolite. *Tectonophysics*, *151*(1–4), 87–105. https://doi.org/10.1016/0040-1951(88)90242-9

Oeser, M., Strauss, H., Wolff, P. E., Koepke, J., Peters, M., Garbe-Schönberg, D., & Dietrich, M. (2012). A profile of multiple sulfur isotopes through the Oman ophiolite. *Chemical Geology*, *312*, 27–46. https://doi.org/10.1016/j.chemgeo.2012.04.008

Orcutt, J. A., Kennett, B. L., & Dorman, L. M. (1976). Structure of the East Pacific Rise from an ocean bottom seismometer survey. *Geophysical Journal International*, *45*(2), 305–320. https://doi.org/10.1111/j.1365-246x.1976.tb00328.x

Pallister, J. S., & Hopson, C. A. (1981). Samail Ophiolite plutonic suite: Field relations, phase variation, cryptic variation and layering, and a model of a spreading ridge magma chamber. *Journal of Geophysical Research*, *86*(B4), 2593–2644. https://doi.org/10.1029/JB086iB04p02593

Perk, N. W., Coogan, L. A., Karson, J. A., Klein, E. M., & Hanna, H. D. (2007). Petrology and geochemistry of primitive lower oceanic crust from Pito Deep: Implications for the accretion of the lower crust at the Southern East Pacific Rise. *Contributions to Mineralogy and Petrology*, *154*(5), 575–590. https://doi.org/10.1007/s00410-007-0210-z

Peters, T., Blechschmidt, I., Krystyn, L., Dumitrica, P., Mercolli, I., El Amin, O., & Al Towaya, A. (2005). *Geological Map of Ibra (1:100,000)*. Sultanate of Oman, Ministry of Commerce and Industry, Sheet NF 40-48 A.

Phipps Morgan, J. P., & Chen, Y. J. (1993). The genesis of oceanic-crust-magma injection, hydrothermal circulation, and crustal rlow. *Journal of Geophysical Research*, *98*(B4), 6283–6297. https://doi.org/10.1029/92jb02650

Prior, D. J., Mariani, E., & Wheeler, J. (2009). EBSD in the earth sciences: Applications, common practice, and challenges. In *Electron backscatter diffraction in materials science* (pp. 345–360). Springer. https://doi.org/10.1007/978-0-387-88136-2_26

Quick, J. E., & Denlinger, R. P. (1993). Ductile deformation and the origin of layered gabbro in ophiolites. *Journal of Geophysical Research*, *98*(B8), 14015–14027. https://doi.org/10.1029/93jb00698

Satsukawa, T., Ildefonse, B., Mainprice, D., Morales, L. F. G., Michibayashi, K., & Barou, F. (2013). A database of plagioclase crystal preferred orientations (CPO) and microstructures—Implications for CPO origin, strength, symmetry and seismic anisotropy in gabbroic rocks. *Solid Earth*, *4*(2), 511–542. https://doi.org/10.5194/se-4-511-2013

Schaeben, H. (1999). The de la Vallée Poussin standard orientation density function. *Texture, Stress, and Microstructure*, *33*(1–4), 365–373. https://doi.org/10.1155/tsm.33.365

Skemer, P., Katayama, I., Jiang, Z., & Karato, S.-i. (2005). The misorientation index: Development of a new method for calculating the strength of lattice-preferred orientation. *Tectonophysics*, *411*(1–4), 157–167. https://doi.org/10.1016/j.tecto.2005.08.023

Sleep, N. H. (1975). Formation of oceanic crust: Some thermal constraints. *Journal of Geophysical Research*, *80*(29), 4037–4042. https://doi.org/10.1029/JB080i029p04037

Teagle, D. A., Ildefonse, B., & Blum, P. (2012). IODP expedition 335: Deep sampling in ODP hole 1256D. *Scientific Drilling*, *13*, 28–34. https://doi.org/10.5194/sd-13-28-2012

VanTongeren, J. A., Hirth, G., & Kelemen, P. B. (2015). Constraints on the accretion of the gabbroic lower oceanic crust from plagioclase lattice preferred orientation in the Samail ophiolite. *Earth and Planetary Science Letters*, *427*, 249–261. https://doi.org/10.1016/j.epsl.2015.07.001

VanTongeren, J. A., Kelemen, P. B., & Hanghøj, K. (2008). Cooling rates in the lower crust of the Oman ophiolite: Ca in olivine, revisited. *Earth and Planetary Science Letters*, *267*(1–2), 69–82. https://doi.org/10.1016/j.epsl.2007.11.034

Vera, E. E., Mutter, J. C., Buhl, P., Orcutt, J. A., Harding, A. J., Kappus, M. E., et al. (1990). The structure of 0-my to 0.2-my old oceanic crust at 9°N on the East Pacific Rise from expanded spread profiles. *Journal of Geophysical Research*, *95*(B10), 15529–15556. https://doi.org/10.1029/JB095iB10p15529

Vernon, R. H. (2000). Review of microstructural evidence of magmatic and solid-state flow. *Visual Geosciences*, *5*(2), 1–23. https://doi.org/10.1007/s10069-000-0002-3

Vollmer, F. W. (1990). An application of eigenvalue methods to structural domain analysis. *The Geological Society of America Bulletin*, *102*(6), 786–791. https://doi.org/10.1130/0016-7606(1990)102<0786:aaoemt>2.3.co;2

Wright, S. I., Nowell, M. M., & Field, D. P. (2011). A review of strain analysis using electron backscatter diffraction. *Microscopy and Microanalysis*, *17*(3), 316–329. https://doi.org/10.1017/s1431927611000055

Yoshinobu, A. S., & Hirth, G. (2002). Microstructural and experimental constraints on the rheology of partially molten gabbro beneath oceanic spreading centers. *Journal of Structural Geology*, *24*(6), 1101–1107. https://doi.org/10.1016/S0191-8141(01)00094-3

Zihlmann, B., Müller, S., Coggon, R. M., Koepke, J., Garbe-Schönberg, D., & Teagle, D. A. H. (2018). Hydrothermal fault zones in the lower oceanic crust: An example from Wadi Gideah, Samail ophiolite, Oman. *Lithos*, *323*, 103–124. https://doi.org/10.1016/j.lithos.2018.09.008